Interaction between the Tidal and Seasonal Variability of the Gulf of Maine and Scotian Shelf Region

ANNA KATAVOUTA AND KEITH R. THOMPSON

Department of Oceanography, Dalhousie University, Halifax, Nova Scotia, Canada

YOUYU LU AND JOHN W. LODER

Bedford Institute of Oceanography, Fisheries and Oceans Canada, Dartmouth, Nova Scotia, Canada

(Manuscript received 18 May 2015, in final form 6 January 2016)

ABSTRACT

As part of a broader study of ocean downscaling, the seasonal and tidal variability of the Gulf of Maine and Scotian shelf, and their dynamical interaction, are investigated using a high-resolution (1/36°) circulation model. The model's seasonal hydrography and circulation, and its tidal elevations and currents, are compared with an observed seasonal climatology, local observations, and results from previous studies. Numerical experiments with and without density stratification demonstrate the influence of stratification on the tides. The model is then used to interpret the physical mechanisms responsible for the largest seasonal variations in the M_2 surface current that occur over, and to the north of, Georges Bank. The model generates a striation pattern of alternating highs and lows, aligned with Georges Bank, in the M_2 surface summer maximum speed in the Gulf of Maine. The striations are consistent with observations by a high-frequency coastal radar system and can be explained in terms of a linear superposition of the barotropic tide and the first-mode baroclinic tide, generated on the north side of Georges Bank, as it propagates into the Gulf of Maine. The seasonal changes in tidal currents in the well-mixed area on Georges Bank are due to a combination of increased sea level gradients, and lower vertical viscosity, in summer.

1. Introduction

Significant advances have been made recently in the development of operational forecast systems for the global ocean (e.g., Chassignet et al. 2009; Molines et al. 2014). For many practical applications (e.g., oil spill trajectory modeling, marine search and rescue), higher spatial resolution forecasts are needed than can be provided by such global systems, particularly on continental shelves where important variability occurs on scales of a few kilometers and less. Another limitation of most global forecast systems is that they do not include tides and thereby miss an important contributor to the high-frequency variability and its influence on the seasonal-mean state.

The present study is part of a larger effort to downscale the results of a global system using a high-resolution regional model of the northwest Atlantic and adjacent shelf seas (Fig. 1). In this study, we focus on the accurate representation of diurnal and semidiurnal tides that are known to be large in the Gulf of Maine and Scotian shelf and can alter the local hydrographic properties, circulation, and sea surface height through processes such as tidal rectification, vertical mixing, and horizontal advection (e.g., Garrett et al. 1978; Loder 1980; Greenberg 1983; Smith 1983; Hannah et al. 2001; Brown 2011). We examine both the effect of the seasonal variation of ocean properties on the tides and the effect of the tides on the seasonal-mean state.

Previous modeling and observational studies (e.g., Marsden 1986; Howarth 1998; Loder et al. 1992; Naimie et al. 1994; Cummins et al. 2000; Ohashi et al. 2009; Chen et al. 2011; Müller et al. 2014) have shown that stratification of the water column can influence tidal elevation and currents over the continental shelf by (i) changing internal and bottom friction, and thus the vertical structure of the currents; (ii) modifying the spatial

Denotes Open Access content.

Corresponding author address: Anna Katavouta, Department of Oceanography, Dalhousie University, 1355 Oxford St., Halifax, NS B3H 4R2, Canada.
E-mail: a.katavouta@dal.ca

DOI: 10.1175/JPO-D-15-0091.1

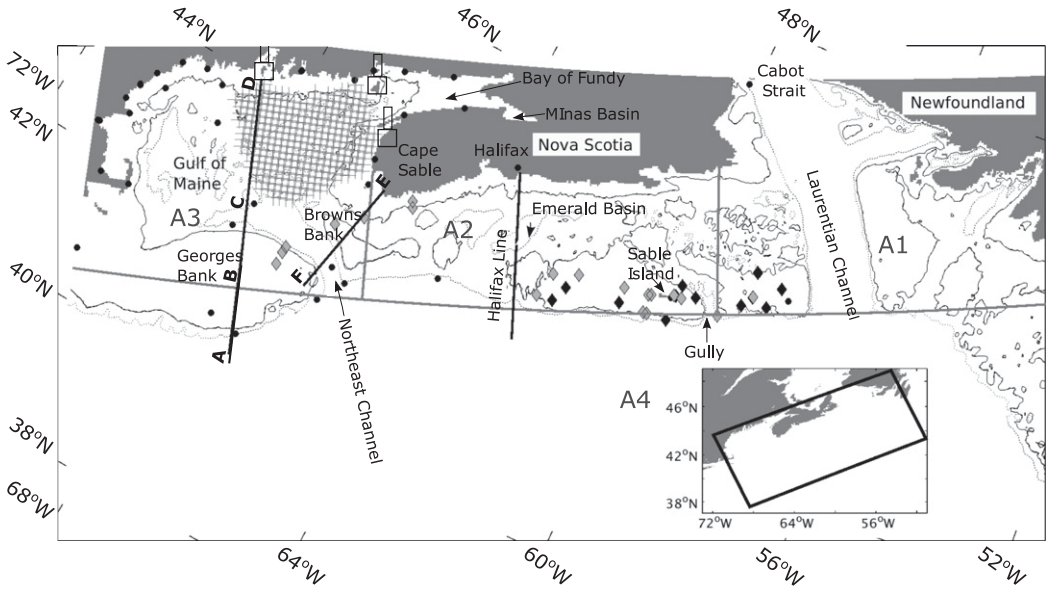

FIG. 1. The GoMSS model domain (inset panel) along with major bathymetric features, place names, and observation locations. The thin black line shows the 100-m isobath, and the dotted line shows the 200-m isobath. The black dots show locations of observations of tidal elevation. The diamonds show locations of moored observations of tidal current (black for winter, gray for summer). The three black lines show five transects that are referred to in the text: Gulf of Maine (A–D), north flank of Georges Bank (B–C), top of Georges Bank to the coast of Maine (B–D), Browns Bank and the Northeast Channel (E–F), and the Halifax Line. The three rectangular shapes show the locations of the three HF radar sites, and the gray mesh shows the area with the HF total velocity data. The domain is separated into four subareas by the thick gray lines: A1 (Laurentian Channel and bounding shelves), A2 (Scotian shelf), A3 (Gulf of Maine), and A4 (deep water).

structure of coastal-trapped wave modes and their propagation along the coastal waveguide; and (iii) generating baroclinic tides. Numerous studies have focused on internal waves generated by surface tides in the Mid-Atlantic Bight and Gulf of Maine (e.g., Halpern 1971; Sawyer 1983; Marsden 1986; LaViolette et al. 1990; Loder et al. 1992; Colosi et al. 2001; Dale et al. 2003; MacKinnon and Gregg 2003; Brown 2011; Nash et al. 2012). Observations from a variety of instruments and platforms have been used (e.g., ADCPs, CTDs, current meters, drifters, and satellites), including, more recently, high-frequency (HF) radar systems that can reveal spatial patterns in near-surface currents with length scales of several kilometers. [See Paduan and Washburn (2013) for an overview of the HF radar technology.]

In the present study, we develop and apply a high-resolution ($^1/_{36}$° grid spacing) model of the Gulf of Maine, Scotian shelf, and adjacent North Atlantic (hereinafter GoMSS) to answer the following questions: Can the model reproduce the observed tidal and seasonal variability of the study area? Does the seasonal variation of density affect tidal elevations and currents, and, if so, is the effect of practical importance and what are the underlying physical mechanisms?

We first show the regional model can reproduce the tides and the main features of the seasonal hydrography and circulation of the study area. We then quantify seasonal changes in tidal elevation and currents. We focus on M_2 because it generally has the strongest tidal currents across the region. We identify, for the first time, a set of spatial ''striations'' in the M_2 summer maximum speed just north of Georges Bank in both the baroclinic model output and HF radar observations. This feature is explained using a linear superposition of the barotropic tide flowing across the north side of Georges Bank and the reflected, phase-locked internal tide. We also identify, and explain, seasonal changes in the M_2 current speed on top of Georges Bank.

The numerical model and the design of the experiments are described in section 2. The model's seasonal-mean hydrography and circulation are briefly discussed in section 3. In section 4, the model's tides are evaluated using current observations from moored meters and an HF radar system operating in the Gulf of Maine, and the striations in M_2 speed are identified. The physical mechanism responsible for the seasonal variation of M_2 tidal currents is discussed in section 5. The results of the study, and their implications, are given in section 6.

2. Numerical model and design of the experiments

The numerical model is based on the ocean component of the Nucleus for European Modeling of the Ocean (NEMO), version 3.1, framework (Madec 2008). The model domain is shown in Fig. 1. GoMSS has a horizontal resolution of approximately 1/36° in longitude and latitude (2.8-km average grid spacing) and 52 z levels with a spacing that varies from 0.7 m near the surface to 233 m at the deepest level (4000 m). Partial cells (Pacanowski and Gnanadesikan 1998) are used to better represent bathymetry. The "variable volume level" (Levier et al. 2007) allows the thickness of the vertical levels to vary with changes in sea surface elevation. The model bathymetry is based mostly on the 2-arc-min Gridded Global Relief Dataset ETOPO2v2 (NOAA, National Geophysical Data Center). Higher-resolution data, provided by Professor Richard Karsten (Acadia University, 2014, personal communication), are used to improve the bathymetry in the inner Gulf of Maine. All depths exceeding 4000 m are clipped at this value. A barotropic–baroclinic time split approach is used. The barotropic and baroclinic time steps are 6 and 180 s, respectively.

The vertical eddy viscosity and diffusivity coefficients are computed using a 1.5 turbulence closure scheme (Gaspar et al. 1990). The horizontal mixing of momentum is parameterized using a scale-selective biharmonic operator with the viscosity set by $-A_M\widetilde{\Delta x}^3$, where $\widetilde{\Delta x}$ is the horizontal grid spacing Δx normalized by its maximum value over the model domain. The mixing term A_M is set equal to $10^9\,\mathrm{m^4\,s^{-1}}$, which is approximately the lower bound that satisfies the grid Reynolds number constraint for the average Δx, centered differencing, and $U = 1\,\mathrm{m\,s^{-1}}$ (Griffies and Hallberg 2000). The horizontal mixing of temperature and salinity is parameterized using a Laplacian scheme along isopycnals with an eddy diffusivity coefficient of $50\,\mathrm{m^2\,s^{-1}}$. A quadratic bottom drag formulation, with a drag coefficient of $r = 0.005$, is used in the horizontal momentum equations. This value was the result of a straightforward sensitivity study in which the fit of the model to tidal elevations in the Gulf of Maine and Scotian shelf was plotted as a function of r.

Momentum and buoyancy fluxes at the ocean surface are calculated using output for six atmospheric variables from a global Climate Forecast System Reanalysis (6-hourly CFSR product; Saha et al. 2010) obtained from the U.S. National Centers for Environmental Prediction (NCEP). The variables are wind at 10 m above the ocean surface, air temperature at 2 m, humidity at 2 m, precipitation, and longwave and incoming shortwave radiation. The atmospheric forcing has approximately 0.3° (~38 km) horizontal resolution. Monthly climatological values of river runoff, based on Co-ordinated Ocean–Ice Reference Experiments (CORE), version 2 (Griffies et al. 2012), are used to specify surface freshwater fluxes in the vicinity of major river mouths.

TABLE 1. Summary of the three runs of GoMSS.

Run name	Period	Density	Atmospheric forcing	Smoothed bathymetry	Tides
Run1	1 yr	Constant	No	No	Yes
Run2	2010 to 2012	Varying	CFSR	No	Yes
Run2s	2010	Varying	CFSR	Yes	Yes

The initial and the lateral boundary conditions of GoMSS (excluding tides) are interpolated from daily temperature, salinity, sea surface height, and horizontal current velocity fields from the 1/12° global Hybrid Coordinate Ocean Model (HYCOM)/Navy Coupled Ocean Data Assimilation (NCODA) analysis system (HYCOM Consortium, www.HYCOM.org). This global system was chosen based on the accuracy of its simulations (e.g., Chassignet et al. 2007, 2009). Five tidal constituents (M_2, S_2, N_2, K_1, and O_1) are also used to drive the model at its lateral open boundaries. (The global system does not include tides.) The tidal elevations and transports are obtained from the finite element solution (FES2004) barotropic global tidal model developed by the Laboratoire d'Etudes en Geophysique et Oceanographie Spatiales (Lyard et al. 2006). FES2004 uses an unstructured grid with a horizontal resolution of about 45 km in the interior of the Gulf of Maine.

Temperature and salinity along GoMSS open lateral boundaries are set to the global system's values when flow enters the domain. A simple upwind advection scheme is used when the flow leaves the domain. A 10 gridpoint sponge layer near the lateral open boundaries is used for both cases. For barotropic currents normal to the open boundary, a Flather radiation scheme (Flather 1976) is applied based on prescribed normal flow and sea surface height. For baroclinic currents, a radiation relaxation-type algorithm (Orlanski forward implicit; Marchesiello et al. 2001) is used within the sponge layer.

Three runs are performed (Table 1). Run1 is for 1 yr and is forced solely by the barotropic tide (no atmospheric forcing). It has no density variations in either space or time. Run2 is a more realistic ocean simulation and is forced by tides and variations in atmospheric forcing and water density (as described in the three previous paragraphs). This run is for 3 yr, from 1 January 2010 to 31 December 2012. Run2s is the same as Run2 except for smoothing of the bathymetry in the Gulf of Maine and a reduced run length (2010 only). The bathymetry was first smoothed by applying a 2D boxcar filter for depths below 100 m in the Gulf of

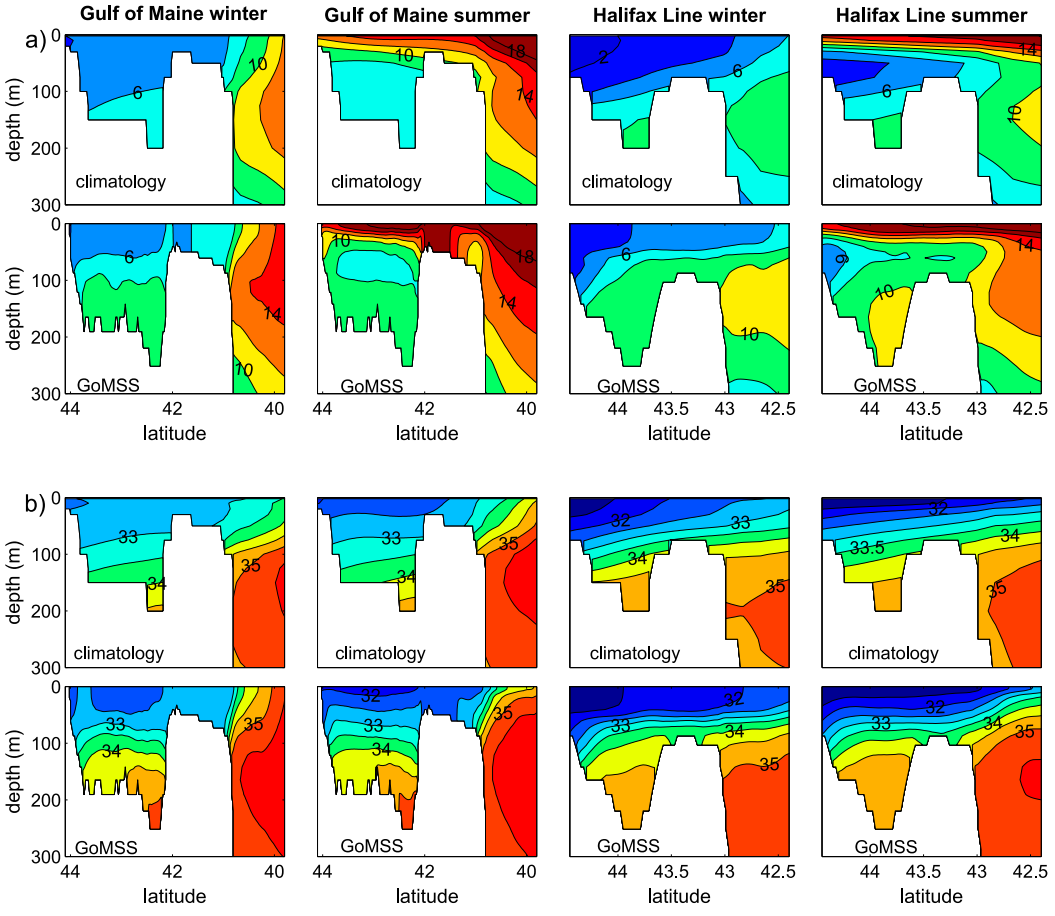

FIG. 2. (a) Temperature (°C) and (b) salinity (psu) for the (top) observed seasonal climatology and (bottom) GoMSS Run2 along the Gulf of Maine (A–D) and the Halifax Line sections (Fig. 1).

Maine and then smoothing the transition at 100 m to eliminate discontinuities.

3. Seasonal variation of stratification and currents

a. Seasonal variation of stratification

The vertical stratification of the Gulf of Maine and Scotian shelf exhibits a pronounced seasonal cycle mainly due to summer surface heating, winter surface cooling, and spatially varying tidal mixing. We now briefly discuss the winter (January–March) and summer (July–September) temperature and salinity fields generated by Run2 and compare them with the observed climatology of Geshelin et al. (1999) and previous studies. The observed monthly climatology is defined on a 1/6° horizontal grid and 32 vertical levels. It is based on all available hydrographic observations up to 1998 from the U.S. National Oceanographic Data Center.

Figures 2 and 3 compare temperature and salinity from Run2 against the observed climatology along two vertical sections (the Halifax Line and a section crossing the Gulf of Maine, A–D; Fig. 1) and for subareas A2 and A3 (Fig. 1). To quantify the level of agreement, the mean and standard deviation of the temperature and salinity discrepancies for all 3D grid points for both sections and subareas A1 to A4 are listed in Table 2 as a function of season and depth.

1) WINTER

On the Scotian shelf (subarea A2) and in the Gulf of Maine (subarea A3), Run2 generates relatively fresh (<34) and cool (<8°C) water above 100 m that extends to the shelf break and cold (<4°C) and fresh (≈31.5) water close to shore on the Scotian shelf, consistent with the outflow from the Gulf of St. Lawrence. These features are in good agreement with the observed climatology (Figs. 2, 3). Run2 also captures the general increase of temperature and salinity with depth due to the intrusion of slope water along the edge of the Scotian shelf and through the Northeast Channel (e.g., Brown and Beardsley 1978; Smith et al. 1978). Run2 simulates the saline (≈34.5),

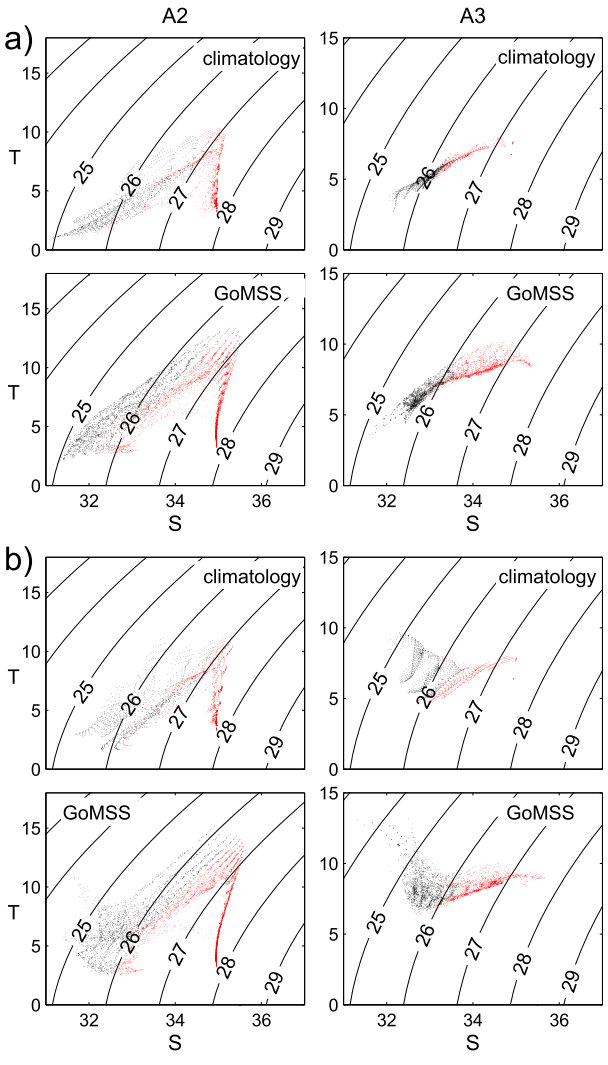

FIG. 3. *T*–*S* diagrams for (a) winter and (b) summer for the (top) observed climatology and (bottom) Run2 below 50 m. The columns of panels correspond to subareas A2 and A3 defined in Fig. 1. Black dots are for depths 50–100 m, and red dots are for depths greater than 100 m. Temperature is in °C, and salinity is in practical salinity units. Run2 results are shown for every fifth model grid point for better visualization.

warm (8°–10°C) water in the Emerald Basin below 100 m, consistent with the observed climatology and previous studies (Petrie and Drinkwater 1993; Loder et al. 2003).

On the shelf (cross-shelf sections and subareas A1–A3), the standard deviations of the observation–model differences of temperature and salinity are less than 1.19°C and 0.37, respectively (Table 2). For the offshelf subarea A4, the standard deviations for both temperature and salinity are larger than those on the shelf, reaching up to 1.43°C and 0.44, respectively (Table 2). This is mainly because the water over the slope is a highly variable mixture of waters from the Gulf Stream and the Labrador Current and also because of the effect of advection due to current meandering and eddies (e.g., McLellan 1957; Gatien 1976; Csanady and Hamilton 1988).

2) SUMMER

Run2 develops a near-surface, warm fresh layer on the Scotian shelf and in the Gulf of Maine due to increased surface heating and freshening of upstream water (Fig. 2). This near-surface layer confines the colder water to intermediate depths (40–100 m) on the Scotian shelf consistent with the observed climatology and previous studies (e.g., Smith et al. 1978; Loder et al. 1997, 2003). On top of Georges Bank, the summer surface layer extends to the bottom in Run2 (Fig. 2) due to the mixing generated by strong tidal currents (Garrett et al. 1978), consistent with observations (e.g., Flagg 1987). Figure 3 shows that Run2 generates warmer (>5°C) water between 50 and 100 m in the Gulf of Maine due to intensified tidal mixing with upper-layer water, consistent with the climatology and earlier observationally based studies (e.g., Flagg 1987). Furthermore, the Run2 temperature–salinity (*T*–*S*) diagrams for the Gulf of Maine are in good agreement with the observationally based *T*–*S* diagrams of Hopkins and Garfield (1979) and Flagg (1987).

Similar to winter, the standard deviations of the observation–model differences for offshelf subarea A4 are generally larger than the standard deviations on the shelf (Table 2).

Overall, Figs. 2 and 3 and Table 2 indicate that GoMSS generates realistic water masses for A2 and A3. Similar analysis (figures not shown) confirms this is also the case for A1 and A4. The model has an overall bias of less than 2°C for temperature and less than 0.35 for salinity. (Run2 is warmer and more saline than the observed climatology.) This bias is not surprising if one takes into account the different periods of the model simulations and the observations, and the large variability in the region on interannual (Hebert et al. 2013) and decadal (Petrie and Drinkwater 1993) time scales. For example, Hebert et al. (2013) noted that 2012 was the warmest year over the last four decades and about 2°C above the mean from 1981 to 2010 at the surface.

b. Seasonal variation of mean currents

We now discuss the winter and summer mean currents across two sections (the Halifax Line and a line radiating from Cape Sable, E–F in Fig. 1). The E–F section crosses Browns Bank and the Northeast Channel. Figure 4 shows the observed and Run2 currents normal to each section for winter and summer. The observed currents are based on the monthly means data archived by the

TABLE 2. Comparison of the seasonal climatology of temperature and salinity based on climatological observations and Run2 along the Gulf of Maine (A–D) and the Halifax Line sections and for the four subareas (A1 to A4) shown in Fig. 1. The values outside the parentheses show mean difference (observed climatology–Run2 climatology) and the values inside the parentheses show the standard deviation of the difference.

Season	Depth range (m)	A–D section	Halifax Line	A1	A2	A3	A4
			Temperature (°C)				
Winter	0–100	−1.02 (1.19)	−1.94 (0.99)	−1.29 (0.45)	−1.98 (0.79)	−1.70 (0.67)	1.27 (1.43)
	101–250	−0.71 (0.98)	−1.18 (0.85)	−1.17 (0.80)	−1.88 (0.77)	−1.95 (0.47)	−1.06 (1.10)
Summer	0–100	−1.88 (1.16)	−1.90 (1.05)	−1.42 (0.66)	−1.89 (1.10)	−1.16 (0.77)	−1.98 (1.48)
	101–250	−1.51 (0.46)	−1.39 (1.02)	−1.62 (1.01)	−1.90 (0.72)	−1.71 (0.44)	−1.40 (1.06)
			Salinity (PSU)				
Winter	0–100	−0.25 (0.37)	−0.05 (0.24)	−0.11 (0.20)	−0.15 (−0.31)	−0.06 (0.28)	−0.19 (0.44)
	101–250	−0.14 (0.35)	−0.08 (0.14)	−0.24 (0.22)	−0.23 (0.18)	−0.35 (0.14)	−0.18 (0.21)
Summer	0–100	0.01 (0.34)	−0.08 (0.32)	−0.09 (0.21)	0.08 (0.34)	−0.10 (0.20)	−0.27 (0.39)
	101–250	−0.17 (0.25)	−0.18 (0.14)	−0.25 (0.23)	−0.22 (0.15)	−0.32 (0.21)	−0.15 (0.20)

Department of Fisheries and Oceans (DFO) (http://www.bio.gc.ca/science/data-donnees/base/data-donnees/odi-eng.php). Only locations with multimonth records between 1960 and 2014 are included. The differences between the Run2 simulations and the observed seasonal-mean currents are quantified in Fig. 4 in terms of two statistical quantities, $\hat{\beta}_1$ and R^2, which come from a linear regression model. This statistical model predicts the observed mean current for a specific location using $\hat{\beta}_0 + \hat{\beta}_1 \mathbf{u}_{\text{mod}}$, where $\mathbf{u}_{\text{mod}}$ is the collocated, modeled mean current; R^2 is the proportion of observed variability that can be predicted by the regression model. See the appendix for

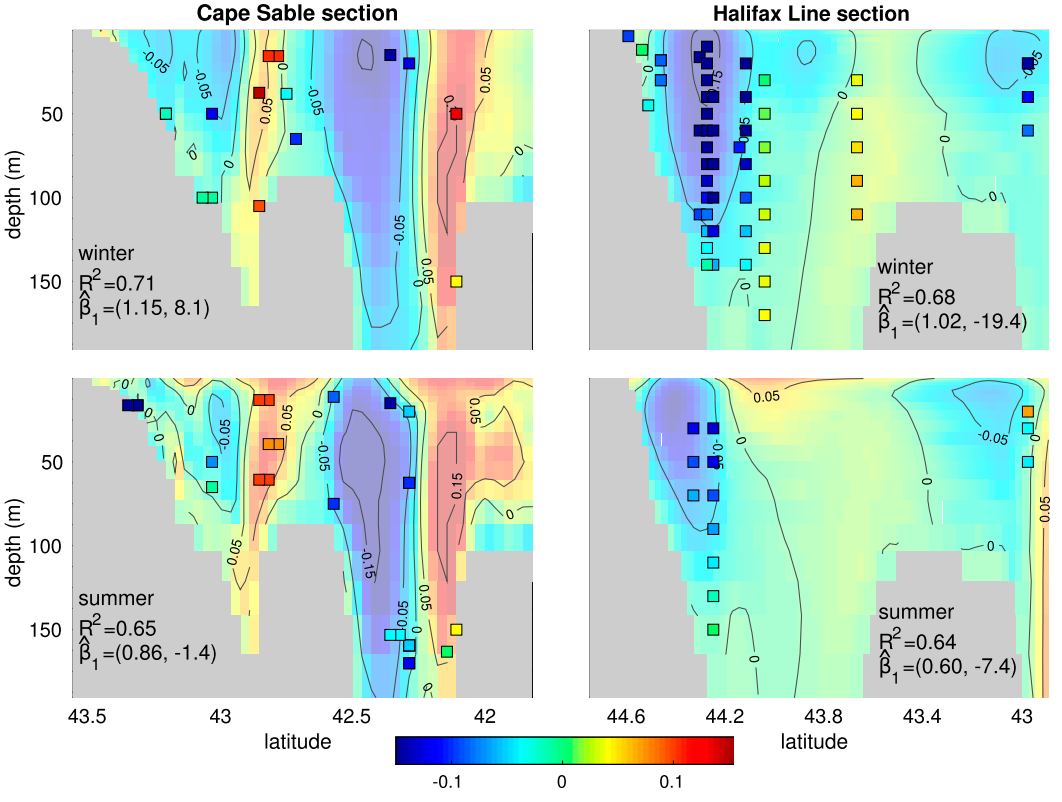

FIG. 4. (top) Model Run2 and observed moored winter and (bottom) summer mean currents ($\mathrm{m\,s^{-1}}$) normal to a section radiating from (left) Cape Sable (E–F) and (right) a section crossing the Scotian shelf (Halifax Line). The boxes show the observed seasonal-mean currents. Positive values in the left (right) panels correspond to flow with a positive eastward (northward) component. The R^2 and $\hat{\beta}_1$ statistics (see the appendix) are given in each panel based on the seasonal-mean current vectors; $\hat{\beta}_1$ is given in polar form (amplitude gain and rotation angle in degrees clockwise).

TABLE 3. The means and standard deviations (in parentheses) of the difference between the observed and Run1 predicted tidal elevation amplitude (cm) and phase (degrees, mapped to ±180°). The observed results are based on data from the 39 locations shown by the black dots in Fig. 1. The first row for each subregion shows the observed mean tidal amplitude A_{obs} for each of the five dominant constituents.

	M_2	N_2	S_2	K_1	O_1
			Bay of Fundy (7 locations)		
A_{obs}	292.8	73.5	42.9	15.5	12.3
$A_{obs} - A_{Run1}$	−8.0 (6.8)	8.2 (10.8)	9.0 (9.2)	6.3 (0.4)	1.7 (0.8)
$\phi_{obs} - \phi_{Run1}$	−12.3 (2.7)	−18.5 (5.9)	19.6 (10.0)	3.2 (1.8)	−19.7 (2.5)
			Gulf of Maine and Georges Bank (27 locations)		
A_{obs}	118.7	26.8	18.7	12.7	10.6
$A_{obs} - A_{Run1}$	−3.4 (9.2)	−1.2 (2.5)	−0.3 (1.8)	5.2 (1.6)	1.7 (1.9)
$\phi_{obs} - \phi_{Run1}$	−14.4 (4.8)	−18.0 (5.5)	8.1 (7.6)	5.7 (3.6)	−14.6 (6.0)
			Scotian shelf (5 locations)		
A_{obs}	47.9	10.1	11.7	6.9	5.5
$A_{obs} - A_{Run1}$	3.3 (7.8)	−0.2 (1.1)	1.0 (1.4)	1.0 (2.0)	−0.2 (0.8)
$\phi_{obs} - \phi_{Run1}$	−5.8 (5.5)	−8.0 (5.6)	18.3 (5.9)	1.0 (13.9)	−2.3 (27.5)

details. Note that the magnitude of the intercept ($\hat{\beta}_0$, not shown) is small, generally less than 0.02 m s^{-1}.

The left panels of Fig. 4 show that, along the Cape Sable transect (E–F), Run2 simulates the observed winter and summer flows with R^2 values of 0.71 and 0.65 and $|\hat{\beta}_1|$ values of 1.15 (about 15% underestimation of the speed) and 0.86 (about 15% overestimation of the speed), respectively. Although Run2 captures the weakening of the flow from the Scotian shelf into the Gulf of Maine, within about 50 km of Cape Sable, during summer, it underestimates its speed by around 0.1 m s^{-1} during winter. Run2 simulates the observed clockwise circulation above Browns Bank that persists throughout the year associated primarily with tidal rectification and mixing (Greenberg 1983; Hannah et al. 2001). It also simulates well the observed circulation along the Northeast Channel: inflow toward the Gulf of Maine along its north side and outflow on its south side. The outflow is part of the clockwise circulation around Georges Bank associated with tidal rectification and frontal circulation; it reaches up to 0.6 m s^{-1} along the northeast side of the bank during summer, consistent with previous studies (e.g., Loder 1980; Butman et al. 1982; Wright and Loder 1985; Naimie et al. 1994; Chen et al. 2001).

The right panels in Fig. 4 show that Run2 simulates well the position and vertical structure of the Nova Scotia Current in winter, although it underestimates the speed (observed and modeled maximum speeds are 0.27 and 0.17 m s^{-1}, respectively). It also captures the observed weakening of this current in summer. In winter, near the edge of Emerald Basin (about 43.7°N), Run2 generates the observed, weak, northward flow that is associated with a cyclonic gyre above the Emerald Basin reported in previous studies (e.g., Han et al. 1997; Hannah et al. 2001). Overall, along the Halifax Line, the skill of Run2 is significant in both winter and summer (R^2 equal to 0.68 and 0.64, respectively). The rotation error is small in summer but reaches almost 20° in winter. In winter Run2 generates realistic speeds ($|\hat{\beta}_1| = 1.02$), while in summer it overestimates the speed by about 40% ($|\hat{\beta}_1| = 0.60$).

Based on currents observed by ADCPs from 2010 to 2012, Hebert et al. (2013) estimated the transport in the Nova Scotia Current across the Halifax Line to be 0.61 and 0.24 Sv (1 Sv ≡ 10^6 m^3 s^{-1}) in winter and summer, respectively. GoMSS generates winter and summer transports of 0.55 and 0.25 Sv, respectively, in good agreement with the observed transports.

Overall, Run2 reproduces the observed influences of the tides on the stratification (e.g., intense mixing on top of Georges Bank) and the circulation (e.g., generation of tidal residual currents around Georges and Brown Banks). The impact of the seasonal variation of density on the tides is discussed in the next section.

4. Seasonal variation of tidal currents

Tidal elevations of the dominant constituents (M_2, N_2, S_2, K_1, and O_1) are relatively well known in the study area (e.g., Greenberg 1979; Daifuku and Beardsley 1983; Moody et al. 1984; Chen et al. 2011) and are simulated well by the FES2004 barotropic model (Lyard et al. 2006) that provides the tidal forcing for GoMSS.

To provide a quantitative assessment of GoMSS, tidal elevations generated by Run1 were compared with observed amplitudes and phases of the above tidal constituents at 39 locations (Fig. 1). The observed amplitudes and phases are based on tidal analyses of sea level time series collected by NOAA and DFO and also amplitudes and phases given by Moody et al. (1984). The error statistics are given in Table 3 for three areas: the Bay of

TABLE 4. Mean and standard deviation (in parentheses) of the differences in tidal elevation amplitude (cm) and phase (degrees) between winter (superscript w) and summer (superscript s) for Run2. Results are based on averages over the whole model domain. The first row shows the mean tidal elevation amplitude for summer.

	M_2	N_2	S_2	K_1	O_1
A^s	53.1	12.2	11.5	5.9	6.0
$A^s - A^w$	1.0 (3.6)	0.2 (0.7)	0.0 (0.4)	0.2 (0.4)	0.0 (0.3)
$\phi^s - \phi^w$	−0.1 (1.0)	0.2 (1.4)	−0.3 (2.0)	0.8 (−4.1)	1.6 (9.3)

Fundy, the Gulf of Maine and Georges Bank, and the Scotian shelf. Table 3 shows that the mean differences are generally small compared to the mean of the observed amplitudes for all areas and constituents. The standard deviation of the amplitude errors is generally small for all areas and constituents (e.g., less than 9.2 cm for M_2).

The tidal elevations generated by Run1 do not vary seasonally in contrast to the Run2 simulations that are influenced by changes in stratification. However, in agreement with Chen et al. (2011), the seasonal changes in the amplitude and phase of Run2 tidal elevations are small (Table 4). More specifically, the seasonal changes in M_2 amplitude are less than 10 cm outside the Bay of Fundy and less than 5 cm outside the Gulf of Maine. The seasonal changes in tidal currents are, however, much larger and are the focus of the rest of this section.

The tidal ellipses for the M_2 surface currents generated by Run2 are shown in Fig. 5 for winter and summer. The ellipses exhibit high spatial variability, with strong tidal currents in the Bay of Fundy (up to 3 m s^{-1}) and over shallow banks (0.9 m s^{-1} over Georges Bank). The ellipses over Georges Bank also show an eccentricity (ratio of minor to major axis) of about 0.7, consistent with observations and theoretical considerations based on vorticity and Sverdrup wave dynamics (Loder 1980; Brown 1984). Over the Scotian shelf, the M_2 currents are negligible near the coast but are stronger over banks on the outer shelf (about 0.2 m s^{-1}). In deep water, the M_2 currents are generally weak as expected, but they are amplified in the vicinity of the Northeast Channel. This amplification is not evident in Run1, and its physical origin is discussed in section 6. It is apparent from Fig. 5 that the size and inclination of the M_2 ellipses vary seasonally over most of the model domain, with the largest changes in the Gulf of Maine and the vicinity of Northeast Channel.

To quantify the seasonal changes (summer minus winter) in the maximum M_2 surface current speeds (i.e., the length of the semimajor axis of the tidal ellipse), we define

$$\delta v = \max_t |\mathbf{u}_s^{M_2}(t)| - \max_t |\mathbf{u}_w^{M_2}(t)|, \qquad (1)$$

where $\mathbf{u}_s^{M_2}(t)$ and $\mathbf{u}_w^{M_2}(t)$ are the time-varying M_2 surface currents at a fixed grid point for summer and winter, respectively. While it may be challenging to observe seasonal differences in M_2 speed from the tidal ellipses shown in Fig. 5, they are clearly evident in the spatial map of δv from Run2 (Fig. 6). Seasonal differences in the maximum current speed exceed 0.1 m s^{-1} in the Gulf of Maine. The differences are largest over Georges Bank, in the Bay of Fundy, and in the vicinity of the Northeast Channel, where the M_2 currents are stronger during summer. The most remarkable features of Fig. 6 are (i) the pattern of maxima and minima (henceforth striations) aligned with the northern side of Georges Bank in the Gulf of Maine and (ii) the δv expression of the summer intensification of M_2 current speed over Georges Bank. The δv striations are due to spatial variability in the summer M_2 tidal current maxima. Although not presented here, the δv striations are evident during each summer of Run2 (2010, 2011, and 2012), where they appear at roughly the same locations and with approximately the same amplitude for each year. To our knowledge this is the first time that such a spatial pattern in the speed of the M_2 tidal current has been noted. No striations are evident at the diurnal frequencies of K_1 and O_1, but they are clearly evident for N_2 and S_2.

a. *Model evaluation using moored current meter observations*

Observed tidal ellipse parameters were obtained from various Bedford Institute of Oceanography technical reports (Drozdowski et al. 2002). We used only those tidal harmonic constants estimated from records that are at least 30 days long and have a known start date [which precluded the use of the parameters listed by Moody et al. (1984)]. Additionally, only observations near the surface (0–20 m) were used. For winter, observations that met the above criteria were available only on the Scotian shelf (15 locations; Fig. 1). For summer, observations were available for Georges Bank, between Cape Sable and Georges Bank, and the Scotian shelf (19 locations; Fig. 1).

To quantify comparisons between the modeled and the observed tidal currents, a new statistic that we call $\tilde{\gamma}^2$ (see the appendix) is used. This nondimensional statistic is the ratio of the mean kinetic energy, averaged over a tidal cycle, of the difference between the observed and predicted tidal current to the mean kinetic energy of the observed tidal current. It takes into account discrepancies in both the amplitude and phase of the tidal currents. Scatterplots of $\tilde{\gamma}^2$ for Run1 and Run2 are shown in Fig. 7 for winter and summer. Note that although Run1 does not vary with season, its $\tilde{\gamma}^2$ values do because the observations vary seasonally. In winter there are locations where $\tilde{\gamma}^2 > 1$ (outside of the gray area). Visual comparison (not shown) of the observed and modeled tidal ellipses at these locations reveals that

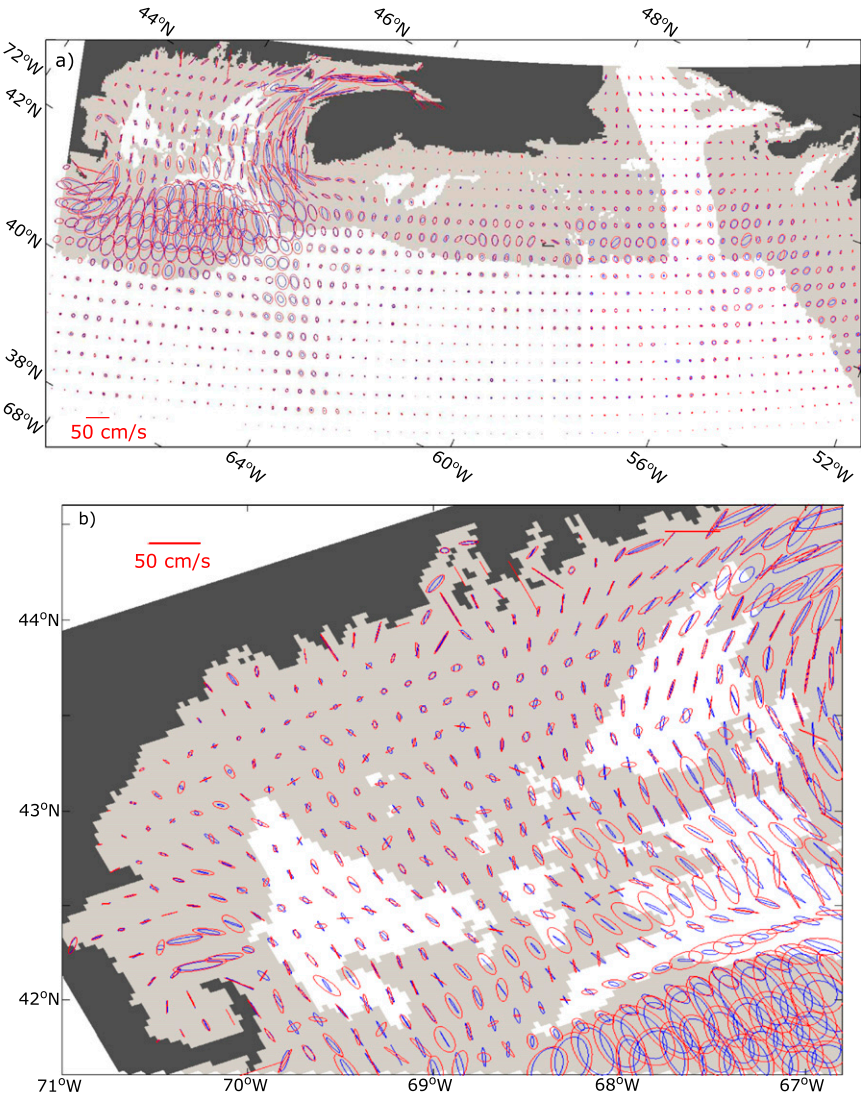

FIG. 5. The M_2 surface tidal current ellipses generated by Run2 for winter (blue) and summer (red). The ellipses are shown every (a) 10 grid points and (b) every 5 grid points. (b) is a zoom of the Gulf of Maine (note the different orientation). The light gray shading shows areas shallower than 200 m.

the large $\tilde{\gamma}^2$ values are due primarily to differences in phase and magnitude, even though the model still captures the overall shape and inclination of the observed ellipses. Figure 7 shows that (i) Run2 has generally smaller $\tilde{\gamma}^2$ than Run1 (most points are below the 1:1 line), indicating that the Run2 tidal current predictions are better than those from Run1 in both winter and summer, and (ii) both Run1 and Run2 have generally smaller $\tilde{\gamma}^2$ for all constituents in summer than in winter, indicating a better fit during summer. Thus, we conclude that Run2 (baroclinic model) is better than Run1 in predicting the observed tidal currents, generally, and it is best during summer. The larger difference (increased spread of points) between the two runs in summer is to be expected because stratification is enhanced at this time of year. Note that some of the discrepancies between the observed and Run2 tidal currents result from interannual variability in the density fields. (The observations and simulations are for different years.)

b. *Model evaluation using HF radar observations*

Surface currents in the Gulf of Maine have been measured for over 10 yr by a Coastal Ocean Dynamics Application Radar (CODAR) SeaSonde HF radar system (Barrick 2008) and have been successfully used in previous studies associated with tidal currents (e.g., Brown

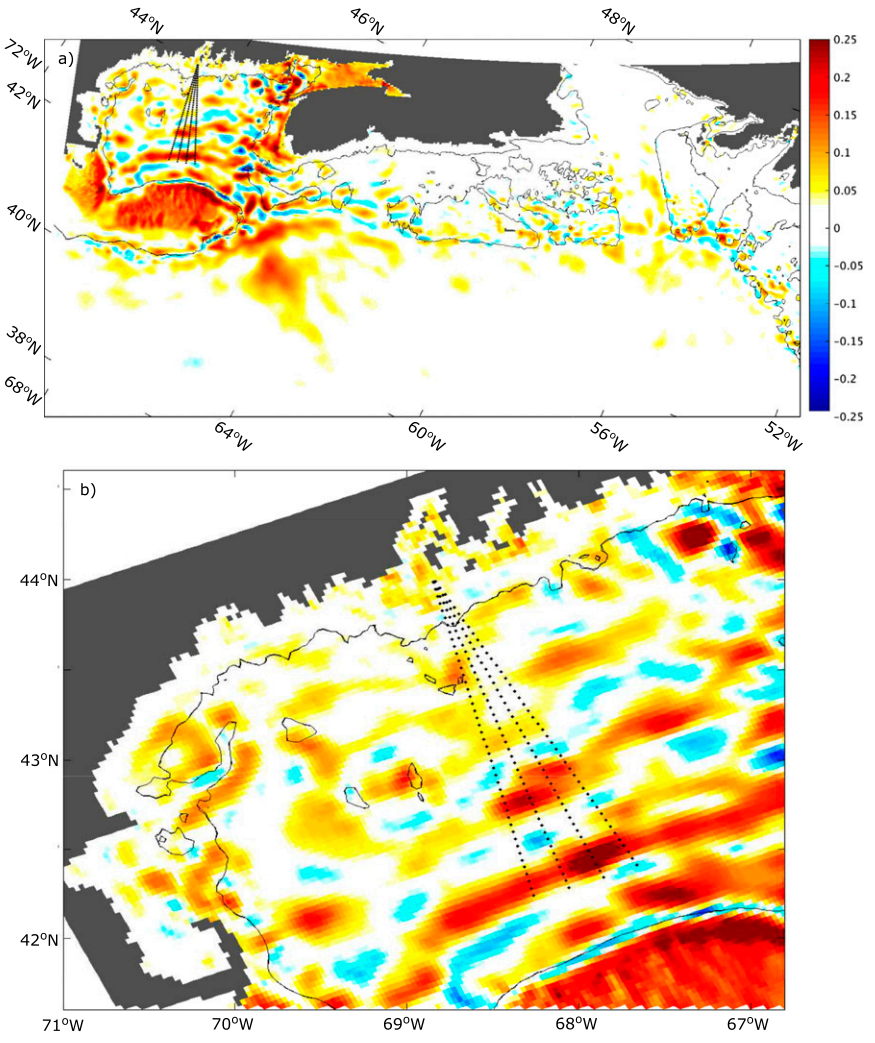

FIG. 6. (a) Seasonal differences in the speed of the M_2 surface current (δv; m s^{-1}), summer–winter based on Run2 for the period 2010–12. (b) A zoom of the Gulf of Maine (note the different orientation). Four HF radar-derived radial current pathways, emanating from the HF radar site at Greens Island, are located by the dotted lines. The thin black line shows the 100-m isobath.

and Marques 2013). The present observing system, supported by the Northeastern Regional Association of Coastal and Ocean Observing Systems (NERACOOS; see Pettigrew et al. 2005, 2010) in partnership with the University of Maine, is composed of three SeaSonde sites located in the eastern Gulf of Maine (Fig. 1). One of the sites is on Greens Island (44.02°N, 68.86°W) at the coastal end of the A–D transect.

Each site has a transmit and receive antenna, radar/radio electronics, and a computer for control, data processing, and logging. The antennae are located as close to the ocean as possible to minimize signal attenuation by propagation over land. The radars transmit concurrently at 4.82 MHz and with a bandwidth of 33 kHz. Timing offsets at the three sites are used to avoid interference with overlapping received backscatter. A comprehensive overview of HF radar-observing technology, and the characteristics of the observations, is given by Paduan and Washburn (2013).

Hourly current data were provided to us by NERACOOS in two forms: velocities resolved along specific radii emanating from a given site (radial data) and vector means estimated from overlapping radial data from the three sites (total data). The radial data are based on 80-min averages (±40 min), output hourly. The radial data were collected at the Greens Island site along four bearings for the summers and winters of 2011 to 2014 (see Fig. 6). The size of the range cell bins is 4.53 km radially and ±2° with respect to direction, defined every 5°. The hourly total velocities were provided on a 10-km grid for the summers and

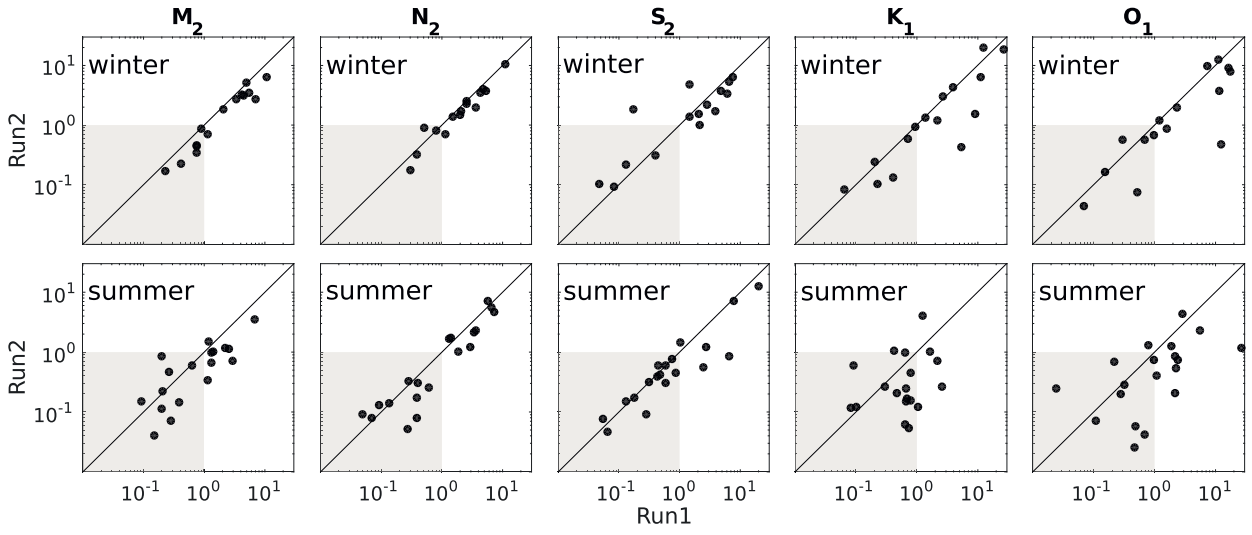

FIG. 7. Evaluation of the surface tidal currents generated by Run2 and Run1. Model simulations are compared with tidal currents estimated from observed mooring data; $\tilde{\gamma}^2$ for Run1 is on the x axis and for Run2 is on the y axis. Results are shown for five tidal constituents. The top row is for winter, and the bottom row is for summer. The gray shading highlights the area for which $\tilde{\gamma}^2 < 1$ for both Run1 and Run2. The 1:1 line is shown by the black diagonal line.

winters of 2013 and 2014. The total velocity vectors were calculated at each grid point by combining intersecting radial current vectors from the three sites using a weighted least squares method. The statistical uncertainties in the hourly total velocity components were calculated using the multiple regression formulae given by Lipa (2003). The median of the hourly statistical uncertainties, across all grid points and times, is 7 cm s^{-1}. We only used hourly total velocities with hourly uncertainties less than 20 cm s^{-1}.

The M_2 tidal ellipses were estimated by harmonic analysis of the hourly total velocity time series for each grid point. We only analyzed gridpoint time series with at least 662 hourly values in summer and 1500 in winter. This ensured the separability of M_2 and N_2 and approximately equal spatial coverage in both seasons (Fig. 1, gridded area). Scatterplots of $\tilde{\gamma}^2$ for the M_2 surface currents predicted by Run2 and Run1, referenced to the observed total velocity data, are shown in the left panels of Fig. 8. The red symbols show the mean $\tilde{\gamma}^2$ for Run1 and Run2, respectively. For both models, the mean $\tilde{\gamma}^2 < 1$ for summer and winter. Run1 has lower mean $\tilde{\gamma}^2$ (red triangle on x axis) than Run2 (red triangle on y axis), and thus, overall, Run1 agrees better with the observations than Run2. However, when the small-scale (<15 km) variability of the Run2 current fields is removed by spatial smoothing, the performance of Run2 improves and matches that of Run1 (overall mean lies on the 1:1 line in the right panels of Fig. 8). By way of contrast, similar spatial smoothing of Run1 leads to no significant differences in its $\tilde{\gamma}^2$ values.

It appears that the poorer agreement of Run2 is related to the smoothing of small-scale features in the observed surface currents by the procedure used to analyze the HF radar data; the total data have an averaging radius of 20 km in the vicinity of the striations, and the distance between a consecutive maximum and minimum in the striations is also about 20 km. The radial data are subject to less spatial smoothing. The upper panel of Fig. 9 shows the difference in the M_2 radial current maximum between summer and winter (similar to δv) for the HF radial observations. The estimated standard errors of the differences are less than 1.5 cm s^{-1} for each of the 46 range bins, implying that the spatial variations in the speed differences shown in Fig. 9 are highly significant from a statistical perspective. (The estimated standard errors were calculated from the standard deviations of the residuals of the tidal analysis and not the formal error estimates of the hourly observations discussed above.) The lower panel of Fig. 9 shows the corresponding results based on tidal analysis of the Run2 surface currents. Overall, the agreement between the results from the HF radial data and Run2 is very encouraging, with the radar data showing maxima and minima that coincide with the locations of the modeled striations.

5. Physical interpretation of the seasonal changes in M_2 tidal speed

a. *North of Georges Bank*

It is well known that the flow of a stratified fluid over abrupt bathymetry (e.g., banks, ridges, shelf edge) can

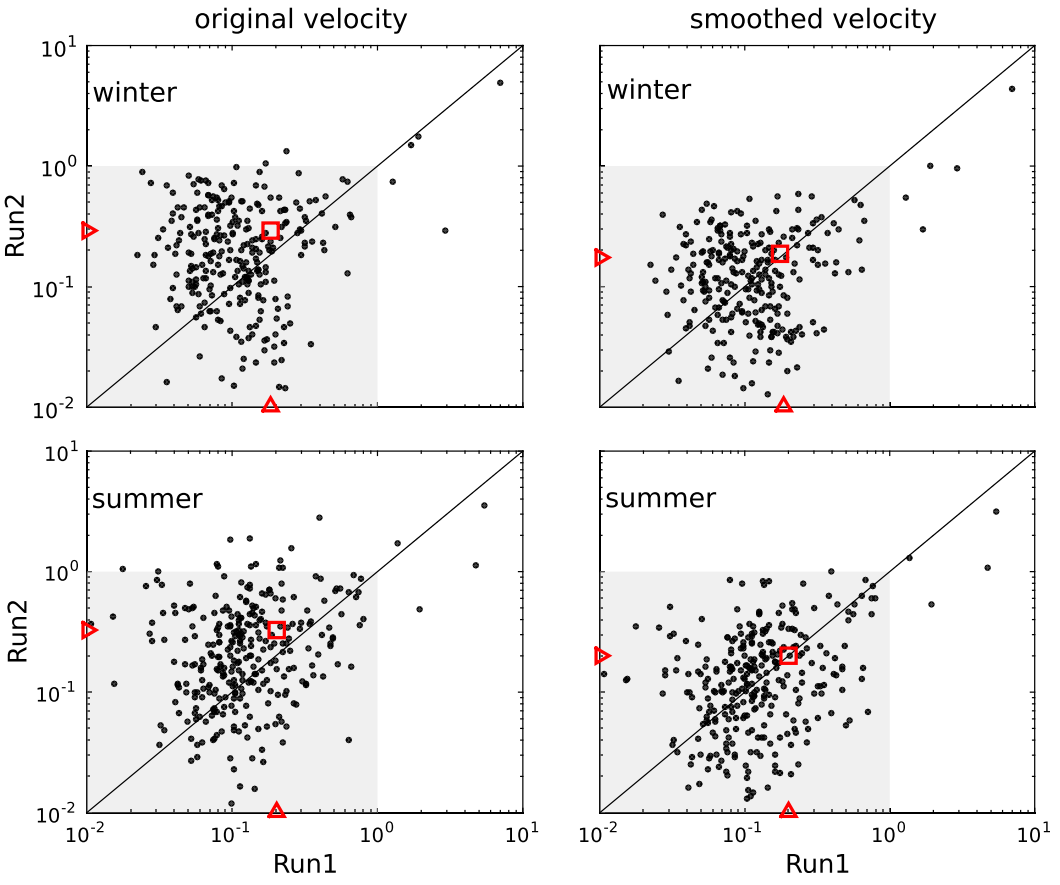

FIG. 8. Evaluation of the M_2 surface tidal currents generated by Run2 and Run1 using the total radar data as observations and the $\tilde{\gamma}^2$ statistic. The left panels are for Run2 and the right panels are for Run2 after spatial smoothing of the surface flow fields as explained in the text. The top panels are for winter and the bottom panels are for summer. The gray shading highlights the area for which $\tilde{\gamma}^2 < 1$ for both Run1 and Run2. The red triangles on x and y axis denote the mean $\tilde{\gamma}^2$ for Run1 and Run2, respectively, and the red square denotes the mean $\tilde{\gamma}^2$. The 1:1 line is shown by the black diagonal line.

generate internal waves (e.g., Baines 1973; Wunsch 1975). When the tide displaces stratified water over sloping bathymetry, it forces internal waves at the tidal frequency that are often referred to as internal tides. Previous studies (e.g., Sawyer 1983; Marsden 1986; LaViolette et al. 1990; Loder and Horne 1991; Loder et al. 1992; Lamb 1994; Dale et al. 2003) have shown that internal tides are generated along the northern flank of Georges Bank. We now show that GoMSS can generate internal tides and then use them to physically explain the striations.

Loder et al. (1992) and Brickman and Loder (1993) proposed a physical mechanism for the generation of internal tides along the northern flank of Georges Bank based on the analysis of current and hydrographic observations along a section crossing the bank edge at 66°48′W. Their explanation has been supported by the idealized, nonlinear, nonhydrostatic numerical modeling study of Lamb (1994) and the subsequent observational study by Dale et al. (2003). Loder and colleagues argued that, during off-bank tidal flow, a depression in the pycnocline develops over the bank edge. This depression subsequently separates into two depressions: one propagating away from and the other propagating toward the bank. The latter depression moves more slowly because it is moving against the off-bank tidal flow. This depression becomes trapped near the bank edge and becomes narrower and deeper as the off-bank flow strengthens. The propagation speed of the (mode 1) internal wave is always larger than the tidal flow in the deep water off the bank, and so the second depression propagates away from the bank during both the flood and ebb tide, analogous to the well-known propagation of internal tides from the shelf edge into the deep ocean observed in many regions (e.g., Wunsch 1975).

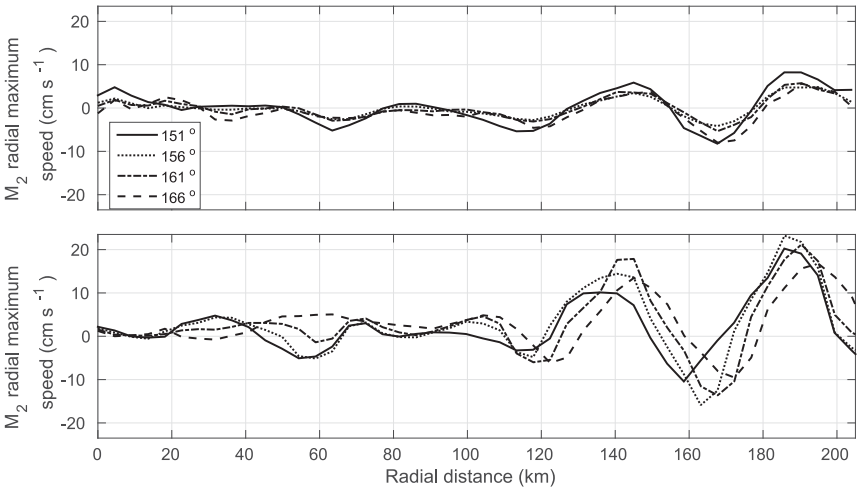

FIG. 9. Spatial distributions of the seasonal (summer–winter) difference in the radial M_2 tidal surface current amplitude (top) as measured by the HF radar site at Greens Island and (bottom) modeled by Run2. Each line corresponds to one of the four radial spokes shown in Fig. 6. The legend shows the angle of each radial spoke with respect to north, measured clockwise. The radial current speeds are estimated from observations from 2011 to 2014, and the Run2 results are for 2010–12. The *x* axis shows radial distance (km) from Greens Island.

To show GoMSS can generate internal waves along the northern flank of Georges Bank during off-bank flow, the vertical structure of hourly snapshots of Run2 density over a typical tidal cycle is shown in Fig. 10. (Analysis of temperature and salinity leads to the same conclusions.) The snapshots are for a typical summer M_2 tidal cycle along a section (B–C, Fig. 1) that crosses the northern flank of Georges Bank about 60 km west of the Loder et al. (1992) observation line. Each pixel corresponds to a model grid cell. For the first six panels, the flow is off bank and the tidal front is advected toward the right (i.e., northward, off the bank). As the off-bank tidal flow strengthens, the isopycnals move downward and a depression develops near the bank edge that propagates northward, away from the bank. The behavior of the model is broadly consistent with the conclusions of Loder et al. (1992) and Brickman and Loder (1993). One difference is that Run2 does not have a depression propagating onto the bank along section B–C. The reason is that stratification does not extend as far onto the bank to the west of the Loder et al. (1992) measurement line, as shown by observations during summer (e.g., Fig. 5 in Naimie et al. 1994).

Another view of the tidal variability generated by Run2 during summer is given by Fig. 11, which shows the time evolution of density near the pycnocline, along a section running from Georges Bank to the coast of Maine (section B–D; Fig. 1). The bottom panels are Hovmöller diagrams of the density anomaly at a depth of 20 m from 10 to 14 July 2010 for Run2 (left panel) and Run2s (right panel). The middle panels show the section's bathymetry (Georges Bank on the left), and the top panels show the maximum M_2 speed during winter and summer. Note the striations are clearly evident in the maximum speed in summer (but not in winter). According to the Run2 Hovmöller diagram, the speed of the propagation of signals away from the northern flank of Georges Bank toward the coast of Maine is about $0.93\,m\,s^{-1}$. This speed is similar to the speed of northward-propagating internal waves (about $1\,m\,s^{-1}$) observed by LaViolette et al. (1990) in ocean photographs taken from the space shuttle and in the ballpark of the cruder estimate (from a single mooring in fall) of $0.4–0.7\,m\,s^{-1}$ by Marsden (1986).

Based on the above, we conclude that GoMSS does generate internal tides along the north edge of Georges Bank, with the observed speed of propagation (away from the bank) even though it is a hydrostatic model.

The Run2 Hovmöller diagram suggests that the speed of the internal waves is not uniform and that the speed changes in regions of variable bathymetry (cf. the middle-left and bottom-left panels in Fig. 11). The Hovmöller diagram for Run2s (bottom-right panel in Fig. 11) shows that the speed of the internal tide is more uniform, highlighting the important effect of local changes in bathymetry on the propagation of internal waves north of Georges Bank. It is important to note, however, that the striations in M_2 surface speed remain in the results from Run2s (top-right panel of Fig. 11), indicating that they are not due to local variations in bathymetry.

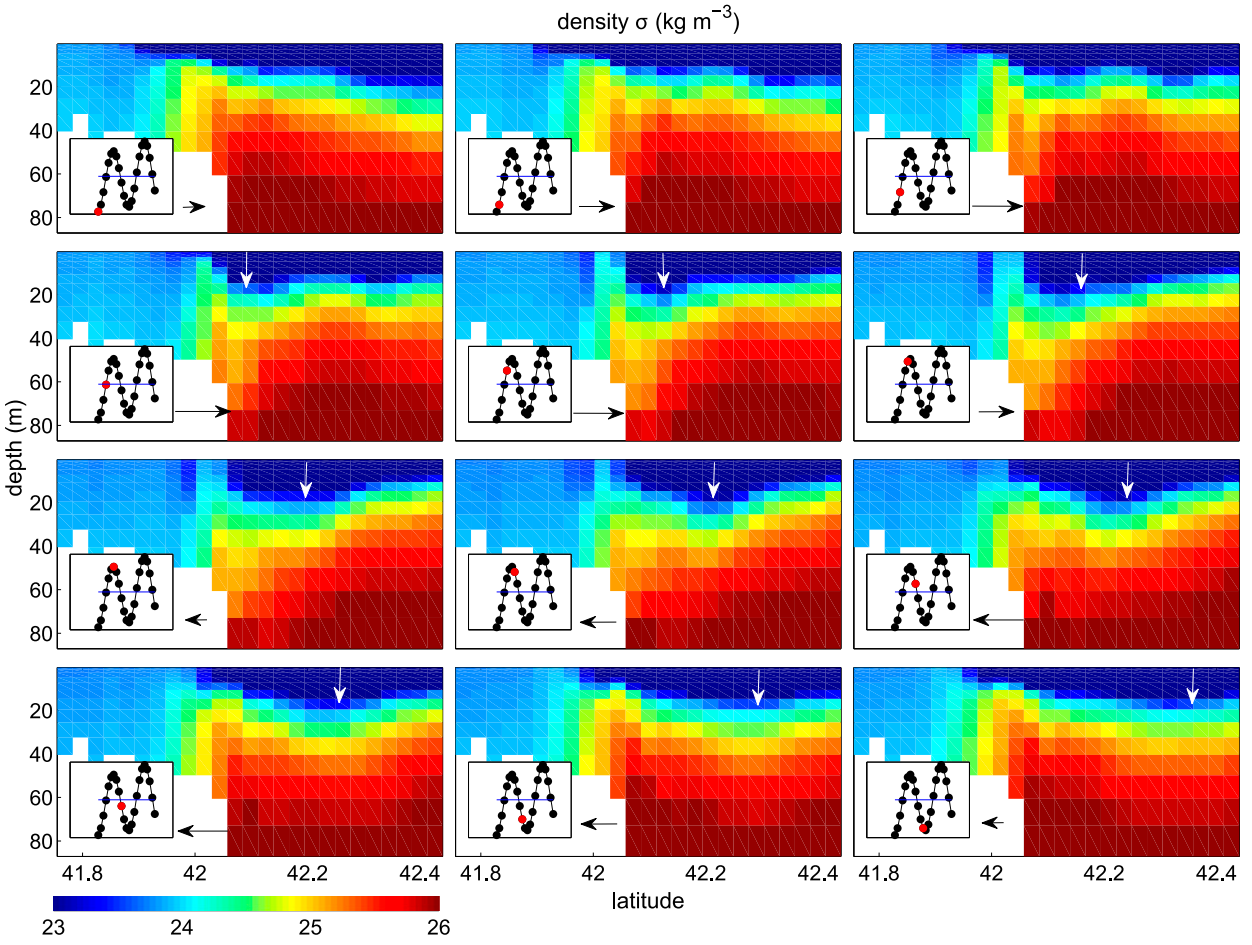

FIG. 10. Hourly snapshots of density from Run2 over a complete M_2 tidal cycle during 10 Jul 2010, along a vertical section north of Georges Bank (B–C; Fig. 1). The insets are time series of tidal elevation at the north edge of the bank, and the red dot shows the snapshot's position in the tidal cycle. The black arrows at the bottom of each panel show the barotropic tidal current strength and direction at the north edge of Georges Bank, toward or away from the bank. The white arrow shows the position of the depression discussed in the text.

To explain physically the summer striations, consider the idealized model of St. Laurent et al. (2003) of internal tide generation by barotropic tidal flow, at frequency ω, over a step in the seafloor (Fig. 12, bottom panels). The water depth to the left and right of the step are denoted by H and $(1 - \delta)H$, respectively, where δ is the normalized height of the step. The ridge normal barotropic flow to the left and right of the step are assumed large scale and of the form $U_0\cos(\omega t)$ and $(1 - \delta)U_0\cos(\omega t)$, respectively. To allow for stratification, St. Laurent et al. (2003) assumed the background density field has a constant buoyancy frequency N. Under the assumption of a rigid lid, linear and hydrostatic flow, and $f < \omega < N$, where f is the inertial frequency, St. Laurent et al. (2003) derived explicit expressions for the baroclinic component of the flow by requiring continuity of horizontal and vertical velocity directly above the step and zero horizontal flow at the vertical edge of the step. Their solutions are expressed in terms of infinite sums of baroclinic modes propagating away from the step in both directions. After nondimensionalizing time by ω^{-1}, the vertical coordinate by H, and the horizontal coordinate by H/α, where $\alpha = \sqrt{(\omega^2 - f^2)/(N^2 - \omega^2)}$ is the wave slope, the horizontal baroclinic velocity depends on only one parameter (the nondimensional step height δ) after normalization by U_0 (i.e., amplitude of the barotropic flow).

Typical output from the St. Laurent et al. (2003) model is shown in the left panels of Fig. 12, assuming $\delta = 1/\sqrt{2}$. The solution has been generated using the first $n = 2000$ baroclinic modes. The bottom panel shows the step and a snapshot of the perturbation density at $t = 0$. The density changes are largest along the characteristic paths emanating from the top of the step, as expected (St. Laurent et al. 2003). The upper panel shows the amplitudes of the barotropic and baroclinic

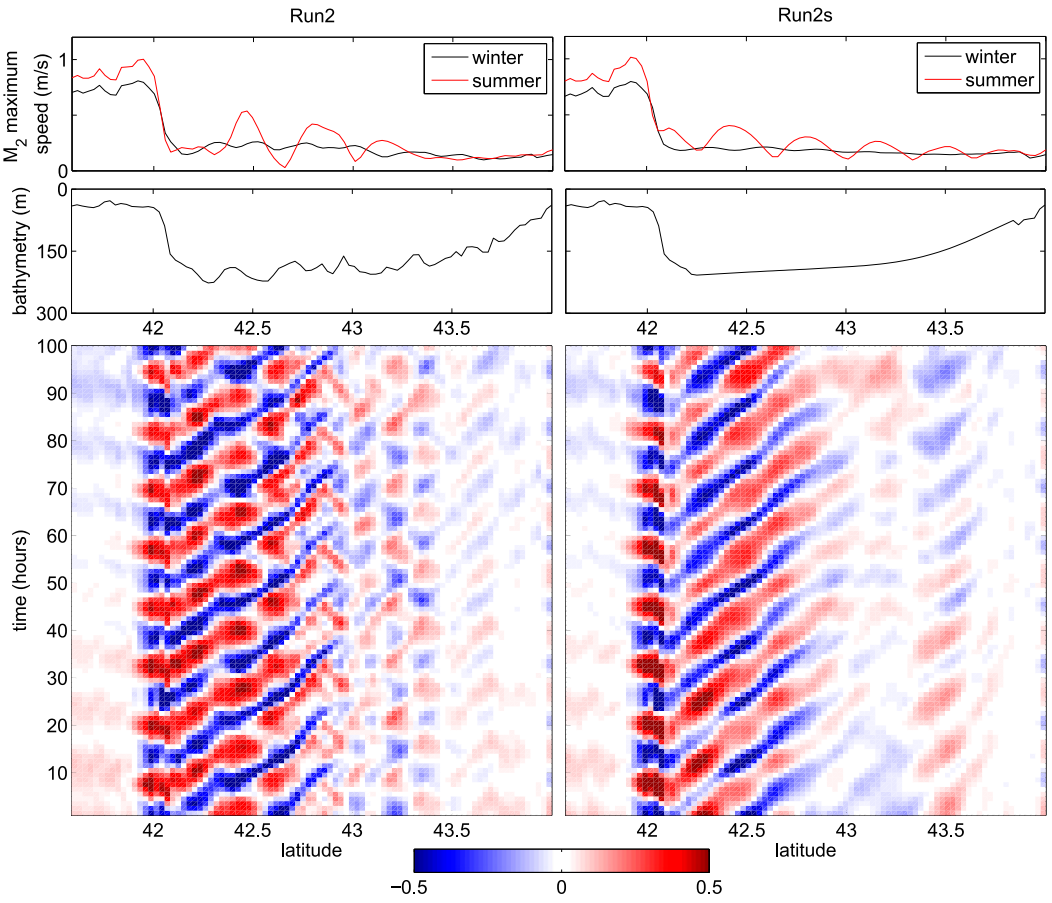

FIG. 11. Simulated tidal variations along a section running from the top of Georges Bank to the coast of Maine (B–D; Fig. 1): (left) Run2 and (right) Run2s. The top panels show the maximum M_2 speed at the surface during summer and winter along the section. The middle panels show the underlying bathymetry (smoothed bathymetry shown in the right panel). The bottom panels are Hovmöller diagrams of the density anomaly (kg m^{-3}) at 20-m depth, defined over eight M_2 tidal cycles between 10 and 14 Jul 2010.

components of horizontal flow at the surface and the amplitude of the total surface flow. As expected, the baroclinic amplitude (blue line) is high in the vicinity of locations where the rays coming from the top of the step reflect from the sea surface. The superposition of the time-varying barotropic flow and the surface baroclinic flow modifies the spatial structure of the amplitude of the surface current (red line) and results in alternating locations where the amplitude of the total surface flow is zero and where the amplitude of the total surface flow is equal to the sum of the barotropic and baroclinic amplitudes. This is because the baroclinic and barotropic components are out of phase at $xH/\alpha = -1, -3, \ldots$ and the amplitudes must be subtracted to get the amplitude of the total flow. Conversely, the baroclinic and barotropic components are in phase when $xH/\alpha = -2, -4, \ldots$, and the amplitudes are additive.

The phase speed of the baroclinic modes varies as the reciprocal of their mode number. Thus, one might expect the higher modes to be dissipated close to the generation region, that is, the step. To illustrate the effect of dissipation, we have generated the solution using only the first baroclinic mode ($n = 1$). The bottom-right panel of Fig. 12 clearly indicates the propagation of this mode in the density perturbation. The top-right panel shows that the total velocity amplitude (red line) has a sinusoidal-like spatial structure (but is not a perfect sinusoid) reminiscent of the striations discussed earlier.

In light of the above, assume the total surface flow in the deep water away from the northern edge of Georges Bank can be approximated by the linear superposition of the barotropic flow and a forced, first baroclinic mode:

$$U_T(x,t) = U_0 \cos(\omega t) + U_1 \cos(\omega t + kx),$$

where U_1 is the amplitude of the baroclinic flow, and k is the associated wavenumber. The total flow can be written

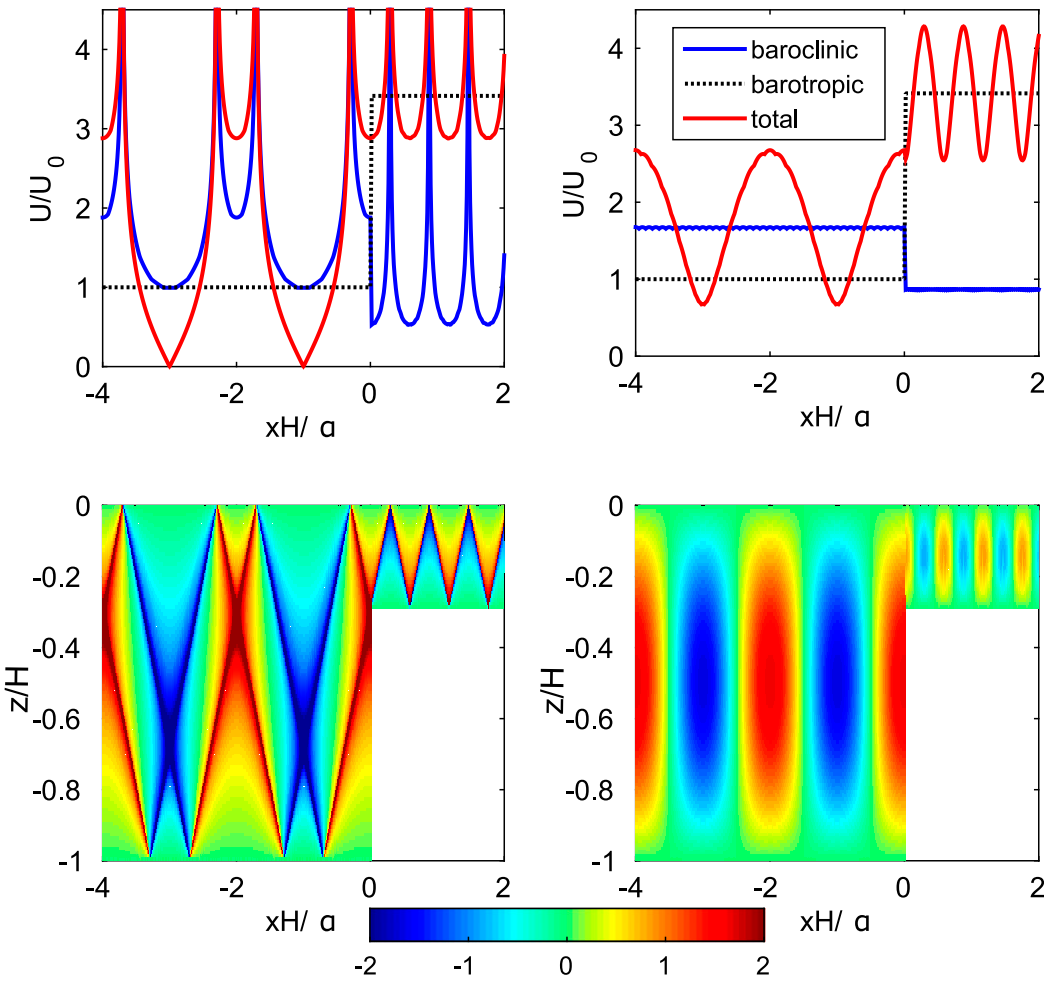

FIG. 12. Predictions of perturbation density and amplitude of surface velocity by the St. Laurent et al. (2003) model. (top) The amplitudes of the barotropic velocity (dashed black line), baroclinic surface velocity (blue line), and total surface velocity (red line). (bottom) The step and snapshots of perturbation density at $t = 0$. The left panels were calculated using $n = 2000$ baroclinic modes. The right panels were calculated using $n = 1$ baroclinic mode. The nondimensional step height is $\delta = 1/\sqrt{2}$.

in the form $U_T(x, t) = A(x)\cos[\omega t + \phi(x)]$, where the spatially varying amplitude and phase are given by

$$A(x) = \sqrt{U_0^2 + U_1^2 + 2U_0U_1\cos(kx)}$$

$$\phi(x) = \arctan\left[\frac{U_1\sin(kx)}{U_0 + U_1\cos(kx)}\right]. \qquad (2)$$

If $U_0 > U_1$ ($U_1 > U_0$), it follows from (2) that $A(x)$ will range between $U_0 \pm U_1$ ($U_1 \pm U_0$) with distance from the bank. For the special case $U_0 = U_1$, the barotropic and baroclinic components will cancel [$A(x) = 0$] when $x = \pi/k, 3\pi/k, \ldots$. In general, (2) predicts spatial variations in $A(x)$ with a spacing equal to the wavelength of the baroclinic surface tidal current like the ones predicted by the St. Laurent et al. (2003) model (Fig. 12). Additionally, (2) shows that the larger the difference between U_0 and U_1, the closer $A(x)$ is to a perfect sinusoid.

The linear superposition of the phase-locked barotropic and baroclinic tides provides a simple physical explanation for the striations in M_2 surface speed plotted in Fig. 9. A similar argument was used by Ray and Mitchum (1996) to explain spatial variations in the amplitude of M_2 tidal elevations observed by altimeters. From Fig. 9, we estimate the spacing between the striations to be about 40 km. Taking ω to be the M_2 tidal frequency, we obtain a phase speed of $0.9\,\mathrm{m\,s^{-1}}$, in good agreement with the internal tide speed from the Hovmöller plots and also the independent observational estimates of LaViolette et al. (1990).

b. Top of Georges Bank

The top of Georges Bank remains vertically well-mixed throughout the year (Fig. 2), and so there is no generation or propagation of baroclinic tides in this region. Throughout the year, the phase of the M_2 current ellipses generated by Run2 changes by less than 10° from top to bottom (around 60 m). These qualitative features are generally consistent with previous studies (e.g., Brown 1984; Marsden 1986; Loder et al. 1992), although available measurements (from water depths of 45–85 m) indicate larger phase differences (e.g., Moody et al. 1984; Loder et al. 1992). Figure 6 indicates an increase in the M_2 current amplitude of about 0.1 m s^{-1} on top of the bank during summer. Vertical profiles for each season (not shown) indicate that the M_2 current speed is stronger throughout the water column, and has more shear in summer compared to winter.

Prandle (1982) proposed an idealized, linear, barotropic model of the vertical structure of tidal currents based on a constant eddy viscosity A_v and a linear bottom drag formulation (coefficient r). The model is formulated in the frequency domain in terms of rotary tidal currents and provides a useful dynamical framework for interpreting the tidal ellipses described in the previous paragraph. In it, the tidal ellipses are forced by a periodically varying local sea level gradient; r primarily influences the amplitude of the modeled tidal currents, and A_v influences their vertical structure.

The amplitude of the sea level gradient forcing, calculated directly from the output of Run2, is higher in summer by about 50% (10%) in the along-bank (cross bank) direction. The vertical eddy viscosity used in GoMSS depends on wind and bottom stress, surface wave breaking, shear and buoyancy production, and vertical convection. A large, fixed value (10 m^2 s^{-1}) is used if the column becomes gravitationally unstable (due, for example, to surface cooling). Because the heat loss during winter favors vertical convection, the net effect is that the eddy viscosity is larger in winter than summer.

The Prandle model, forced by sea level gradients from Run2, can accurately diagnose the seasonal changes in the overall amplitude, vertical structure, and phase of the M_2 tidal ellipses on top of Georges Bank using the seasonally varying sea level gradient and plausible values of A_v (higher in winter). We conclude that the seasonal variation of the M_2 tidal current on top of Georges Bank is due to a combination of stronger sea level gradients and lower eddy viscosity in summer compared to winter.

6. Summary and discussion

Based on comparisons of model output with a climatology, seasonal-mean currents based on observations, and previous studies, we conclude that GoMSS captures many of the well-known, large-scale features of the seasonal-mean hydrography and circulation of the Gulf of Maine and Scotian shelf. The effect of the tides on the seasonal-mean state was clearly evident in the model's simulation of well-mixed water mass on top of Georges Bank and the generation of tidally rectified flows around shallow banks (e.g., Georges and Browns Banks).

GoMSS simulations of tidal elevation and currents are generally consistent with observations from coastal tide gauges, fixed moorings, and land-based HF radar systems. Comparison of output from Run2 and Run1 showed that tides vary with season due to seasonal changes in stratification. For M_2, the seasonal changes in tidal elevation amplitude are less than 10 cm outside the Bay of Fundy and less than 5 cm outside the Gulf of Maine. The effect of seasonal stratification on tidal currents is relatively more important in the Gulf of Maine and the deep water adjacent to the Northeast Channel; for both locations the maximum M_2 tidal currents in summer can exceed the collocated winter maxima by more than 0.1 m s^{-1}.

GoMSS generates an interesting pattern of alternating highs and lows in the M_2 surface summer maximum speed in the Gulf of Maine aligned with the north side of Georges Bank (the striations). This pattern is observed in HF radar radial velocities. The striations are absent in winter and for diurnal tidal frequencies. This is, to our knowledge, the first time that such a pattern has been explicitly identified and observed in this region. The striations are linked to the generation of internal tides along the north side of Georges Bank and their propagation toward the coast of Maine. An idealized model based on St. Laurent et al. (2003) was used to show that the striations are caused by the linear superposition of the barotropic and forced, phase-locked baroclinic tide. Seasonal changes in tidal currents were also identified on top of Georges Bank and explained in terms of seasonal changes in sea level gradients and vertical eddy viscosity.

Our results reinforce the high potential of coastal HF radar for providing synoptic maps of surface current with spatial resolution of tens of kilometers (or less). Turning to future work, we note that although GoMSS simulates the location of the striations consistent with HF radar radial velocities, it overestimates their amplitude. To further explore the striations, a higher-resolution, possibly nonhydrostatic, model is

required, complemented by a well-designed summer field program.

More work is also required to explain some of the features in the map of tidal ellipses (Fig. 5) and δv (Fig. 6). One interesting feature is the region of relatively strong M_2 currents in the deep water offshore of the Northeast Channel in both summer and winter. This feature is absent from Run1 and is thus associated with the density field. Patterns resembling the striations are evident in the vicinity of the Northeast Channel (Fig. 6). We consider their explanation to be beyond the scope of this study but suggest an account should be taken of (i) the complex bathymetry, resulting in internal tides coming from multiple directions; (ii) the highly variable density field in this region; and (iii) more than just the first baroclinic mode. Another result worthy of further investigation is the cause of the seasonal variation in the sea level gradient on top of Georges Bank and its possible relationship with seasonal changes in the resonant frequency of the Gulf of Maine and Bay of Fundy system.

Acknowledgments. We thank Drs. Neil Fisher and Neal Pettigrew for providing the radial and total HF radar observations and related information and Dr. Jean-Philippe Paquin for help in setting up the NEMO model. We thank Dr. David Greenberg and two anonymous reviewers for many constructive and insightful comments. This work was supported by the Ocean Tracking Network (OTN) Canada through a Strategic Network Grant (NETGP 375118-08) from the Natural Sciences and Engineering Research Council of Canada (NSERC), and the Marine Environmental Observation Prediction and Response Network (MEOPAR), which was established through the Canadian federal Networks of Centres of Excellence Program.

APPENDIX

Measuring Model Fit

To quantify the overall accuracy of the Run2 seasonal-mean currents, the following linear regression model was used:

$$\mathbf{u}_{\text{obs}} = \beta_0 + \beta_1 \mathbf{u}_{\text{mod}} + \varepsilon, \tag{A1}$$

where $\mathbf{u}_{\text{obs}}$ and $\mathbf{u}_{\text{mod}}$ denote the collocated observed and modeled seasonal-mean currents, respectively, and ε denotes the error. The variables and regression coefficients are complex with the real and imaginary parts corresponding to eastward and northward components of flow, respectively. The complex regression coefficient β_1 scales and rotates the model currents by the same amount at each location to best fit the observations. If $|\beta_1| < 1$, the ocean model overestimates the observed current speeds and vice versa. The intercept β_0 is a constant flow that must be added to all predictions by the regression model to best fit the observations. It can be thought of as a large-scale flow field not captured by the ocean model.

The estimates of β_0 and β_1 are obtained using complex least squares and are denoted by $\hat{\beta}_0$ and $\hat{\beta}_1$. The predicted mean flow is then given by $\hat{\mathbf{u}} = \hat{\beta}_0 + \hat{\beta}_1 \mathbf{u}_{\text{mod}}$, and we use the following statistic to quantify model fit:

$$R^2 = \frac{\sum_{i=1}^{N_{\text{obs}}} |\hat{\mathbf{u}}|_i^2}{\sum_{i=1}^{N_{\text{obs}}} |\mathbf{u}_{\text{obs}}|_i^2}, \tag{A2}$$

where N_{obs} is the number of observed seasonal-mean currents; R^2 corresponds to the proportion of kinetic energy of the observed mean flow, across all observation locations, that is accounted by Run2. It is constrained to be between 0 and 1. If the sample mean of $\mathbf{u}_{\text{obs}}$ and $\mathbf{u}_{\text{mod}}$ are zero, R^2 corresponds to the usual coefficient of determination used to quantify the fit of a regression model.

To compare the observed and model tidal ellipses, we define the following statistic:

$$\tilde{\gamma}^2 = \frac{\int_0^p |\tilde{\mathbf{u}}_{\text{obs}}(t) - \tilde{\mathbf{u}}_{\text{mod}}(t)|^2 \, dt}{\int_0^p |\tilde{\mathbf{u}}_{\text{obs}}(t)|^2 \, dt}, \tag{A3}$$

where p is the period of the tidal constituent of interest, and $\tilde{\mathbf{u}}_{\text{obs}}(t)$ and $\tilde{\mathbf{u}}_{\text{mod}}(t)$ are time-varying tidal current vectors at frequency $2\pi/p$ that have been generated using the observed and modeled tidal amplitudes and phases. The term $\tilde{\gamma}^2$ is bounded below 0 and unbounded above. If $\tilde{\gamma}^2 \ll 1$, the model predicts the observed tidal currents with small error; specifically for $\tilde{\gamma}^2 = 0$, the error is zero and the ocean model predicts the observed tidal currents perfectly. If $\tilde{\gamma}^2 \gg 1$, the errors are, on average, much larger than the observations, and the ocean model has no useful skill. If $\tilde{\gamma}^2 = 1$, then a prediction of no tidal current will fit the observations as well as the predictions from the ocean model.

We assess the performance of Run1 and Run2 surface tidal currents in terms of the $\tilde{\gamma}^2$ statistic in Figs. 7 and 8. Each point in the plot corresponds to a specific location where the Run1 and Run2 $\tilde{\gamma}^2$ values are compared. If a point falls below the 1:1 line (black line in Figs. 7 and 8), then the model corresponding to the y axis fits the observations better. If the points cluster near the 1:1 line, the performance of the two runs is similar.

REFERENCES

Baines, P. G., 1973: The generation of internal tides by flat-bump topography. *Deep-Sea Res. Oceanogr. Abstr.*, **20**, 179–205, doi:10.1016/0011-7471(73)90050-8.

Barrick, D. E., 2008: 30 years of CMTC and CODAR. *Proc. IEEE/OES Ninth Working Conf. on Current Measurement Technology*, Charleston, SC, IEEE, 131–136, doi:10.1109/CCM.2008.4480856.

Brickman, D., and J. W. Loder, 1993: Energetics of the internal tide on northern Georges Bank. *J. Phys. Oceanogr.*, **23**, 409–424, doi:10.1175/1520-0485(1993)023<0409:EOTITO>2.0.CO;2.

Brown, W. S., 1984: A comparison of Georges Bank, Gulf of Maine and New England shelf tidal dynamics. *J. Phys. Oceanogr.*, **14**, 145–167, doi:10.1175/1520-0485(1984)014<0145:ACOGBG>2.0.CO;2.

——, 2011: Winter variability in the western Gulf of Maine: Part 1: Internal tides. *Dyn. Atmos. Oceans*, **52**, 224–249, doi:10.1016/j.dynatmoce.2011.03.004.

——, and R. C. Beardsley, 1978: Winter circulation in the western Gulf of Maine: Part 1. Cooling and water mass formation. *J. Phys. Oceanogr.*, **8**, 265–277, doi:10.1175/1520-0485(1978)008<0265:WCITWG>2.0.CO;2.

——, and G. M. Marques, 2013: Transient tidal eddy motion in the western Gulf of Maine, part 1: Primary structure. *Cont. Shelf Res.*, **63**, S90–S113, doi:10.1016/j.csr.2012.08.018.

Butman, B., and Coauthors, 1982: Recent observations of the mean circulation on Georges Bank. *J. Phys. Oceanogr.*, **12**, 569–591, doi:10.1175/1520-0485(1982)012<0569:ROOTMC>2.0.CO;2.

Chassignet, E. P., H. E. Hurlburt, O. M. Smedstad, G. R. Halliwell, P. J. Hogan, A. J. Wallcraft, R. Baraille, and R. Bleck, 2007: The HYCOM (Hybrid Coordinate Ocean Model) data assimilative system. *J. Mar. Syst.*, **65**, 60–83, doi:10.1016/j.jmarsys.2005.09.016.

——, and Coauthors, 2009: US GODAE global ocean prediction with the Hybrid Coordinate Ocean Model (HYCOM). *Oceanography*, **22**, 64–75, doi:10.5670/oceanog.2009.39.

Chen, C., R. Beardsley, and P. J. S. Franks, 2001: A 3-D prognostic numerical model study of the Georges Bank ecosystem. Part I: Physical model. *Deep-Sea Res. II*, **48**, 419–456, doi:10.1016/S0967-0645(00)00124-7.

——, and Coauthors, 2011: Tidal dynamics in the Gulf of Maine and New England shelf: An application of FVCOM. *J. Geophys. Res.*, **116**, C12010, doi:10.1029/2011JC007054.

Colosi, J. A., R. C. Beardsley, J. F. Lynch, G. Gawarkiewicz, C. S. Chiu, and A. Scotti, 2001: Observations of nonlinear internal waves on the outer New England continental shelf during the summer Shelfbreak Primer study. *J. Geophys. Res.*, **106**, 9587–9601, doi:10.1029/2000JC900124.

Csanady, G. T., and P. Hamilton, 1988: Circulation of slopewater. *Cont. Shelf Res.*, **8**, 565–624, doi:10.1016/0278-4343(88)90068-4.

Cummins, P. F., D. Masson, and M. G. G. Foreman, 2000: Stratification and mean flow effects on diurnal tidal currents off Vancouver Island. *J. Phys. Oceanogr.*, **30**, 15–30, doi:10.1175/1520-0485(2000)030<0015:SAMFEO>2.0.CO;2.

Daifuku, P. R., and R. C. Beardsley, 1983: The K_1 tide on the continental shelf from Nova Scotia to Cape Haterras. *J. Phys. Oceanogr.*, **13**, 3–17, doi:10.1175/1520-0485(1983)013<0003:TKTOTC>2.0.CO;2.

Dale, A. C., D. S. Ullman, J. A. Barth, and D. Hebert, 2003: The front on the northern flank of Georges Bank in spring: 1. Tidal and subtidal variability. *J. Geophys. Res.*, **108**, 8009, doi:10.1029/2002JC001327.

Drozdowski, A., C. G. Hannah, and J. W. Loder, 2002: The northwest Atlantic tidal current database. Ocean Sciences Division, Fisheries and Oceans Canada, Bedford Institute of Oceanography, Canadian Tech. Rep. of Hydrography and Ocean Sciences 222, 42 pp. [Available online at http://www.dfo-mpo.gc.ca/Library/265853.pdf.]

Flagg, C. N., 1987: Hydrographic structure and variability. *Georges Bank*, R. H. Backus and D. W. Bourne, Eds., MIT Press, 108–124.

Flather, R. A., 1976: A tidal model of the northwest European continental shelf. *Mem. Soc. Roy. Sci. Liege*, **10**, 141–164.

Garrett, C. J., J. R. Keeley, and D. A. Greenberg, 1978: Tidal mixing versus thermal stratification in the Bay of Fundy and Gulf of Maine. *Atmos.–Ocean*, **16**, 403–423, doi:10.1080/07055900.1978.9649046.

Gaspar, P., Y. Grégoris, and J.-M. Lefevre, 1990: A simple eddy kinetic energy model for simulation of the oceanic vertical mixing: Tests at station Papa and long-term upper ocean study. *J. Geophys. Res.*, **95**, 16 179–16 193, doi:10.1029/JC095iC09p16179.

Gatien, M. G., 1976: A study in the slope water region south of Halifax. *J. Fish. Res. Board Can.*, **33**, 2213–2217, doi:10.1139/f76-270.

Geshelin, Y., J. Sheng, and R. J. Greatbatch, 1999: Monthly mean climatologies of temperature and salinity in the western North Atlantic. Ocean Sciences Division, Fisheries and Oceans Canada, Bedford Institute of Oceanography, Canadian Data Rep. of Hydrography and Ocean Sciences 153, 62 pp. [Available online at http://www.dfo-mpo.gc.ca/Library/240168.pdf.]

Greenberg, D. A., 1979: A numerical model investigation tidal phenomena in the Bay of Fundy and Gulf of Maine. *Mar. Geod.*, **2**, 161–187, doi:10.1080/15210607909379345.

——, 1983: Modelling the mean barotropic circulation in the Bay of Fundy and Gulf of Maine. *J. Phys. Oceanogr.*, **13**, 886–904, doi:10.1175/1520-0485(1983)013<0886:MTMBCI>2.0.CO;2.

Griffies, S. M., and R. W. Hallberg, 2000: Biharmonic friction with Smagorinsky-like viscosity for use in large-scale eddy-permitting ocean models. *Mon. Wea. Rev.*, **128**, 2935–2946, doi:10.1175/1520-0493(2000)128<2935:BFWASL>2.0.CO;2.

——, M. Winton, B. Samuels, G. Danabasoglu, S. Yeager, S. Marsland, and H. Drange, 2012: Dataset and protocol for the CLIVAR WGOMD Coordinate Ocean-Sea Ice Reference Experiment (COREs). WCRP Rep. 21, 20 pp. [Available online at http://data1.gfdl.noaa.gov/~nnz/mom4/COREv2/doc/CORE_notes_15feb2012.pdf.]

Halpern, D., 1971: Semidiurnal tides in Massachusetts Bay. *J. Geophys. Res.*, **76**, 6573–6584, doi:10.1029/JC076i027p06573.

Han, G., C. G. Hannah, J. W. Loder, and P. C. Smith, 1997: Seasonal variation of the three-dimensional mean circulation over the Scotian shelf. *J. Geophys. Res.*, **102**, 1011–1025, doi:10.1029/96JC03285.

Hannah, C. G., J. A. Shore, J. W. Loder, and C. E. Naimie, 2001: Seasonal circulation on the western and central Scotian shelf. *J. Phys. Oceanogr.*, **31**, 591–615, doi:10.1175/1520-0485(2001)031<0591:SCOTWA>2.0.CO;2.

Hebert, D., R. Pettitas, D. Brickman, and M. Dever, 2013: Meteorological, sea ice and physical oceanographic conditions on the Scotian shelf and in the Gulf of Maine during 2012. Canadian Science Advisory Secretariat Research Doc. 2013/058, 51 pp. [Available online at http://www.dfo-mpo.gc.ca/Csas-sccs/publications/resdocs-docrech/2013/2013_058-eng.pdf.]

Hopkins, T. S., and N. Garfield, 1979: Gulf of Maine intermediate water. *J. Mar. Res.*, **37**, 103–139.

Howarth, M. J., 1998: The effect of stratification on tidal current profiles. *Cont. Shelf Res.*, **18**, 1235–1254, doi:10.1016/S0278-4343(98)00042-9.

Lamb, K. G., 1994: Numerical experiments of internal wave generation by strong tidal flow across a finite amplitude edge. *J. Geophys. Res.*, **99**, 843–864, doi:10.1029/93JC02514.

LaViolette, P. E., D. R. Johnson, and D. A. Brooks, 1990: Sunglitter photographs of Georges Bank and the Gulf of Maine from the space shuttle. *Oceanography*, **3**, 43–49, doi:10.5670/oceanog.1990.21.

Levier, B., A. M. Treguier, G. Madec, and V. Garnier, 2007: Free surface and variable volume in the NEMO code. MERSEA IP Rep. WP09-CNRS-STR-03-1A, 46 pp. [Available online at http://www.nemo-ocean.eu/content/download/258/1661/file/NEMO_vvl_report.pdf.]

Lipa, B. J., 2003: Uncertainties in SeaSonde current velocities. *Proc. IEEE/OES Seventh Working Conf. on Current Measurement Technology*, San Diego, CA, IEEE, 95–100, doi:10.1109/CCM.2003.1194291.

Loder, J. W., 1980: Topographic rectification of tidal currents on the sides of Georges Bank. *J. Phys. Oceanogr.*, **10**, 1399–1416, doi:10.1175/1520-0485(1980)010<1399:TROTCO>2.0.CO;2.

——, and E. P. W. Horne, 1991: Skew eddy fluxes as signatures of non-linear tidal current interactions, with application to Georges Bank. *Atmos.–Ocean*, **29**, 517–546, doi:10.1080/07055900.1991.9649415.

——, D. Brickman, and E. P. W. Horne, 1992: Detailed structure of currents and hydrography on the northern side of Georges Bank. *J. Geophys. Res.*, **97**, 14 331–14 351, doi:10.1029/92JC01342.

——, G. Han, C. G. Hannah, D. A. Greenberg, and P. C. Smith, 1997: Hydrography and baroclinic circulation in the Scotian shelf region: Winter versus summer. *Can. J. Fish. Aquat. Sci.*, **54**, 40–56, doi:10.1139/f96-153.

——, C. G. Hannah, B. D. Petrie, and E. A. Gonzalez, 2003: Hydrographic and transport variability on the Halifax section. *J. Geophys. Res.*, **108**, 8003, doi:10.1029/2001JC001267.

Lyard, F., F. Lefevre, T. Letellier, and O. Francis, 2006: Modelling the global ocean tides: Modern insight from FES2004. *Ocean Dyn.*, **56**, 394–415, doi:10.1007/s10236-006-0086-x.

MacKinnon, J. A., and M. C. Gregg, 2003: Shear and baroclinic energy flux on the summer New England shelf. *J. Phys. Oceanogr.*, **33**, 1462–1475, doi:10.1175/1520-0485(2003)033,1462:SABEFO.2.0.CO;2.

Madec, G., 2008: NEMO ocean engine. Institut Pierre-Simon Laplace Note du Pole de Modélisation 27, 300 pp.

Marchesiello, P., J. C. McWilliams, and A. Shchepetkin, 2001: Open boundary conditions for long-term integration of regional oceanic models. *Ocean Modell.*, **3**, 1–20, doi:10.1016/S1463-5003(00)00013-5.

Marsden, R. F., 1986: The internal tide on Georges Bank. *J. Mar. Res.*, **44**, 35–50, doi:10.1357/002224086788460157.

McLellan, H. J., 1957: On the distinctness and origin of the slope water off the Scotian shelf and its easterly flow south of the Grand Banks. *J. Fish. Res. Board Can.*, **14**, 213–239, doi:10.1139/f57-011.

Molines, J. M., B. Barnier, T. Penduff, A. M. Treguier, and J. Le Sommer, 2014: ORCA12.L46 climatological and interannual simulations forced with DFS4.4: GJM02 and MJM88. Drakkar Group Experiment Rep. GDRI-DRAKKAR-2014-03-19, 49 pp. [Available online at http://www.drakkar-ocean.eu/publications/reports.]

Moody, J. A., and Coauthors, 1984: Atlas of tidal elevation and current observations on the northeast American continental shelf and slope. USGS Bulletin 1611, 122 pp. [Available online at https://pubs.er.usgs.gov/publication/b1611.]

Müller, M., J. Y. Cherniawsky, M. G. G. Foreman, and J.-S. von Storch, 2014: Seasonal variation of the M_2 tide. *Ocean Dyn.*, **64**, 159–177, doi:10.1007/s10236-013-0679-0.

Naimie, C. E., J. W. Loder, and D. R. Lynch, 1994: Seasonal variation of the three-dimensional residual circulation on Georges Bank. *J. Geophys. Res.*, **99**, 15 967–15 989, doi:10.1029/94JC01202.

Nash, J. D., S. M. Kelly, E. L. Shroyer, J. M. Moum, and T. F. Duda, 2012: The unpredictable nature of internal tides on continental shelves. *J. Phys. Oceanogr.*, **42**, 1981–2000, doi:10.1175/JPO-D-12-028.1.

Ohashi, K., J. Sheng, K. R. Thompson, C. G. Hannah, and H. Ritchie, 2009: Effect of stratification on the tidal circulation over the Scotian shelf and Gulf of St. Lawrence: A numerical study using a three-dimensional shelf circulation model. *Ocean Dyn.*, **59**, 809–825, doi:10.1007/s10236-009-0212-7.

Pacanowski, R. C., and A. Gnanadesikan, 1998: Transient response in a *z*-level ocean model that resolves topography with partial cells. *Mon. Wea. Rev.*, **126**, 3248–3270, doi:10.1175/1520-0493(1998)126<3248:TRIAZL>2.0.CO;2.

Paduan, J. D., and L. Washburn, 2013: High-frequency radar observations of ocean surface currents. *Annu. Rev. Mar. Sci.*, **5**, 115–136, doi:10.1146/annurev-marine-121211-172315.

Petrie, B., and K. Drinkwater, 1993: Temperature and salinity variability on the Scotian shelf and Gulf of Maine 1945–1990. *J. Geophys. Res.*, **98**, 20 079–20 089, doi:10.1029/93JC02191.

Pettigrew, N. R., J. P. Wallinga, F. P. Neville, and K. R. Schlenker, 2005: Gulf of Maine Ocean Observing System (GoMOOS): Current measurement approaches in a prototype integrated ocean observing system. *Proc. IEEE/OES Eighth Working Conf. on Current Measurement Technology*, Southampton, United Kingdom, IEEE, 127–131, doi:10.1109/CCM.2005.1506356.

——, P. C. Fikes, and M. K. Beard, 2010: Advances in the ocean observing system in the Gulf of Maine: Technical capabilities and scientific results. *Proc. OCEANS 2010 IEEE-Sydney*, Sydney, Australia, IEEE, 1–9, doi:10.1109/OCEANSSYD.2010.5603663.

Prandle, D., 1982: The vertical structure of tidal currents and other oscillatory flows. *Cont. Shelf Res.*, **1**, 191–207, doi:10.1016/0278-4343(82)90004-8.

Ray, R. D., and G. T. Mitchum, 1996: Surface manifestation of internal tides generated near Hawaii. *Geophys. Res. Lett.*, **23**, 2101–2104, doi:10.1029/96GL02050.

Saha, S., and Coauthors, 2010: The NCEP climate forecast system reanalysis. *Bull. Amer. Meteor. Soc.*, **91**, 1015–1057, doi:10.1175/2010BAMS3001.1.

Sawyer, C., 1983: Tidal phase of internal-wave generation. *J. Geophys. Res.*, **88**, 2642–2648, doi:10.1029/JC088iC04p02642.

Smith, P. C., 1983: The mean and seasonal circulation off southwest Nova Scotian. *J. Phys. Oceanogr.*, **13**, 1034–1054, doi:10.1175/1520-0485(1983)013<1034:TMASCO>2.0.CO;2.

——, B. Petrie, and C. R. Mann, 1978: Circulation, variability, and dynamics of the Scotian shelf and slope. *J. Fish. Res. Board Can.*, **35**, 1067–1083, doi:10.1139/f78-170.

St. Laurent, L. S., S. Stringer, C. Garrett, and D. Perrault-Joncas, 2003: The generation of internal tides at abrupt topography. *Deep-Sea Res. I*, **50**, 987–1003, doi:10.1016/S0967-0637(03)00096-7.

Wright, D. G., and J. W. Loder, 1985: A depth-dependent study of the topographic rectification of tidal currents. *Geophys. Astrophys. Fluid Dyn.*, **31**, 169–220, doi:10.1080/03091928508219269.

Wunsch, C., 1975: Internal tides in the ocean. *Rev. Geophys. Space Phys.*, **13**, 167–182, doi:10.1029/RG013i001p00167.